Physics-based modeling and experimental investigation of field-assisted manufacturing processes

by

Mingman Sun

B.S., China University of Petroleum, 2013
M.S., China University of Petroleum, 2016

AN ABSTRACT OF A DISSERTATION

submitted in partial fulfillment of the requirements for the degree

DOCTOR OF PHILOSOPHY

Department of Industrial and Manufacturing Systems Engineering
Carl R. Ice College of Engineering

KANSAS STATE UNIVERSITY
Manhattan, Kansas

2022

Abstract

This twofold dissertation focuses on physics-based modeling and experimental investigation of field-assisted manufacturing processes. Part I consists of 5 chapters, which investigates ultrafast laser-assisted micro- and nanofabrication by two-photon polymerization. Chapter 1 thoroughly reviews the principle, materials, and applications of two-photon polymerization with the latest developments. Chapter 2 discusses the model development for two-photon polymerization by a Bessel beam. Chapter 3 describes model validation by comparing SEM-measured and model-predicted polymerized pillar structure diameters. Chapter 4 presents a detailed discussion of the simulated results. Chapter 5 states the future research in utilizing the established model as a practical tool to generate the processing science for volumetric additive manufacturing by two-photon polymerization.

Part II focuses on ultrasonic-assisted manufacturing for biomass-based products. It has 5 chapters that are separate from those in Part I. The investigation creates a new knowledge base on synchronized torrefaction and pelletizing assisted by ultrasonic vibration to utilize renewable and domestically available biomass. Chapter 1 reviews the composition, structure, and properties of lignocellulosic biomass, and states the conventional biomass preprocessing and pretreatment methods. Chapter 2 presents the experimental platforms for ultrasonic vibration amplitude measurement and synchronized ultrasonic torrefaction and pelleting procedure. Chapter 3 describes a physics-based modeling of synchronized ultrasonic torrefaction and pelleting procedure. Chapter 4 and 5 are conclusions and an outlook for bioenergy research, which are essential when making important strategic and operational decisions in biomass energy manufacturing.

Physics-based modeling and experimental investigation of field-assisted manufacturing processes

by

Mingman Sun

B.S., China University of Petroleum, 2013
M.S., China University of Petroleum, 2016

A DISSERTATION

submitted in partial fulfillment of the requirements for the degree

DOCTOR OF PHILOSOPHY

Department of Industrial and Manufacturing Systems Engineering
Carl R. Ice College of Engineering

KANSAS STATE UNIVERSITY
Manhattan, Kansas

2022

Approved by:

Major Professor
Meng Zhang

Copyright

Abstract

This twofold dissertation focuses on physics-based modeling and experimental investigation of field-assisted manufacturing processes. Part I consists of 5 chapters, which investigates ultrafast laser-assisted micro- and nanofabrication by two-photon polymerization. Chapter 1 thoroughly reviews the principle, materials, and applications of two-photon polymerization with the latest developments. Chapter 2 discusses the model development for two-photon polymerization by a Bessel beam. Chapter 3 describes model validation by comparing SEM-measured and model-predicted polymerized pillar structure diameters. Chapter 4 presents a detailed discussion of the simulated results. Chapter 5 states the future research in utilizing the established model as a practical tool to generate the processing science for volumetric additive manufacturing by two-photon polymerization.

Part II focuses on ultrasonic-assisted manufacturing for biomass-based products. It has 5 chapters that are separate from those in Part I. The investigation creates a new knowledge base on synchronized torrefaction and pelletizing assisted by ultrasonic vibration to utilize renewable and domestically available biomass. Chapter 1 reviews the composition, structure, and properties of lignocellulosic biomass, and states the conventional biomass preprocessing and pretreatment methods. Chapter 2 presents the experimental platforms for ultrasonic vibration amplitude measurement and synchronized ultrasonic torrefaction and pelleting procedure. Chapter 3 describes a physics-based modeling of synchronized ultrasonic torrefaction and pelleting procedure. Chapter 4 and 5 are conclusions and an outlook for bioenergy research, which are essential when making important strategic and operational decisions in biomass energy manufacturing.

Table of Contents

List of Figures

List of Tables

Acknowledgements

I appreciate my supervisor, Dr. Meng Zhang, for providing me with the opportunity to explore the exciting field of ultrafast laser photolithography and synchronized ultrasonic torrefaction and pelleting. His patient guidance, depth of knowledge, and willingness to help were invaluable treasure. I learnt from him how to independently tackle research problems, formulate theoretical concepts, and bridge them with practical applications.

I would like to thank Dr. Xiaoming Yu and Dr. Stephen M. Kuebler who introduced me to the interesting world of polymers and photopolymerization. I consider myself lucky to be a part of the collaborative research group and to work with professionals who are genuinely passionate about research. I would also like to thank Dr. Shing I. Chang, Dr. Suprem R. Das, Dr. Donghai Wang, and Dr. Matthew Berg for their guidelines in my research and being an integral part of the dissertation committee.

I acknowledge the support and help that I received from my colleague, Yang Yang. I also graciously acknowledge collaborators, He Cheng, Chun Xia, and Pooria Golvari, for their assistance in modifying the original simulation program and their suggestions for improving the simulation algorithm.

I would like to thank my Department Head, Dr. Bradley Kramer, for his support and encouragement throughout my graduate studies. I would also like to thank the staff of Industrial and Manufacturing Systems Engineering department, Ms. Vicky Geyer, Ms. Deb Harper, and Ms. Danielle Brooks, for their assistance and care.

I would like to express my deep gratitude to my parents Quan Zhou and Zhonggen Sun, for their ever-present and unconditional support and encouragement. They have always been a

source of inspiration for me. Finally, I would like to thank my son Leo Sun, who has always filled my life with blessings of love, peace, and joy.

Part I - Ultrafast Laser-Assisted Fabrication of Micro- and Nano Structures

Typically, TPP systems employ a focused Gaussian beam moved by mechanical or optical means in a photocurable resin. Micro- and nanostructures are built via point-by-point scanning on each predetermined layer. A major disadvantage of conventional TPP is that throughput is slow because the polymerized volume element ("voxel") is small, and a large number ($10^4 - 10^7$) of low-energy laser pulses are needed to polymerize every voxel. To increase both the resolution and the throughput of TPP, research effort has focused on engineering the laser beam wavefront as a flexible and effective means for fabricating complex forms in a single or reduced number of exposures. A Bessel beam is employed in this work because the non-diffractive focus of Bessel beam can have the depth of field significantly longer than the Rayleigh range of a Gaussian beam of a comparable diameter.

Previous studies mainly utilized laser parameters in the weak-pulse regime, where single pulse energies are on the order of 1 nJ. In this regime, a large number of pulses are needed to polymerize the material, so repetition rates are high, up to 100 MHz. The present work considers the strong-pulse regime of TPP, where the laser is operated at low repetition rates (<< 1 MHz) and the pulse energies are high (>> 1 nJ). Because the probability $p_{(abs)}$ for a photoinitiator to absorb two-photons increases with the square of the photon flux φ, two-photon absorption becomes much more efficient with strong pulses (μJ).

This research attempts to answer the following question: For a given photopolymer composition and a laser system with an average input laser power P, what is the most energy-efficient way of delivering the laser energy to create a single polymerized voxel? Energy-efficiency is key to improving fabrication throughput in a process constrained by total optical

power. Results show that 3D structures can be fabricated using a few exposures of strong pulses (μJ). It is more energy-efficient to use fewer and higher-energy pulses in low single pulse energy regime (< 10 μJ), yet this trend reverses when termination by radical-radical recombination becomes more severe in the regime of high single pulse energy (10 μJ - 30 μJ). TPP fabrication in this regime can overcome some fundamental challenges faced by current high-repetition-rate systems, such as low throughput, elevated temperature, beam distortion, and obstruction by previously written structures.

Chapter 1 - Literature Review of Two-Photon Polymerization

1.1. Introduction to Two-Photon Polymerization

Photopolymerization is a technique that utilizes light (visible, ultraviolet, infrared) to initiate and propagate a polymerization reaction to form a solid structure. In the last few decades, photopolymerization additive manufacturing has been rapidly developed in the field of micro-optics, electronics, communications, biomedicine, microfluidic devices, micro-electro-mechanical systems (MEMS) and metamaterials [1]. As the demand for the fabrication of micro/nanostructures from these fields continues increasing, there have been concentrated efforts to develop various micro/nanostructures fabrication technologies like deep UV lithography, electron/ion beam lithography, nano imprint lithography (NIL), and micro stereolithography [2]. Most of these technologies have been successfully applied in the fabrication of two-dimensional nano-patterns and simple three-dimensional microstructures. However, there exist many problems inhibiting their actual performances. For instance, deep UV lithography can fabricate three-dimensional structures but struggle to provide submicron resolution, electron/ion beam lithography can achieve nanoscale resolution but only in the form of two-dimensional structures. Recently, the study of two-photon polymerization (TPP) has sprang up since it was first proposed as an additive manufacturing method [3]. The advantage of TPP is its capability to fabricate arbitrary and ultraprecise three-dimensional microstructures with high resolution not only on the microscopic scale but also on the nanoscale [4].

The physical properties of the laser source, including laser wavelength, pulse energy, pulse duration, repetition rate, and beam profile, strongly impact the nonlinear interaction in the photomaterial and the final formed structure resulting from TPP. Laser wavelength has to be chosen with respect to the spectral sensitivity of the photoinitiator; the pulse energy and the

repetition rate impose limits to the manufacturing speed; the beam profile influences the shape and size of the polymerized volumetric pixels (voxel) [5-7]. It is generally known that the knowledge of voxel size is critical, since voxel is the building block of any microstructure and essentially controls the spatial resolution of the process. Therefore, a mathematical approach is needed to help understanding the voxel size and how it is affected by extracting the role of various process and material-dependent parameters, so that researchers can have a better understanding of the polymerization kinetics and thermodynamics during additive manufacturing. The objective of this project is to establish and apply a multi-physics modeling framework for two-photon polymerization additive manufacturing that connects light-matter interaction, polymerization chemistry, and 3D object development in the system.

1.1.1. Two-Photon Absorption

Two-photon absorption (TPA) is the fundamental principle of TPP. Different from single photon absorption (SPA) employed in conventional stereolithography, TPA process absorbs two photons when the photoinitiator molecules transit from a lower energy level to a higher energy level [8]. There exist two different kinds of mechanisms for TPA: sequential excitation and simultaneous excitation. The former involves a real intermediate state A* of the absorbing species. This intermediate state becomes populated by the first photon, and it can act as the starting point for the absorption of the second one, as shown in Figure 1(a). The real intermediate state A* has a well-defined lifetime, typically 10^{-4} to 10^{-9} s, so the second photon must be absorbed by the same particle within the lifetime of A* to cause the photochemical change [9]. In the other mechanism, there is no real intermediate state involved, but a virtual state A* is created by the interaction of the absorbing species with the first photon as shown in Figure 1(b). Only if the second photon arrives within the virtual state lifetime, about 10^{-15} s, can it be

absorbed. Therefore, it is apparent that high intensities are required for TPA process, which usually requires an ultrafast laser with high peak intensity such as mode-locked Ti:Sapphire lasers [10].

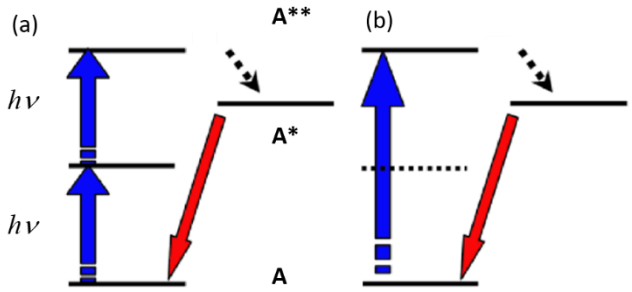

Figure 1. Scheme of (a) sequential excitation and (b) simultaneous excitation. Copyright Optical Materials Express 10, no. 11 (2020): 2928-2943.

Specifically, when a laser beam is focused on a point with a high numerical aperture (NA) objective lens, as shown in Figure 2(a), the density of photons decreases with the distance away from focal plane, but the total number of photons at every cross section remain constant (Figure 2(b)). The constant number of photons at every cross section precludes optical sectioning by exploiting the linear response of the materials to the light intensity based on single photon absorption. Therefore, the resin is solidified completely in the illuminated resin even beyond the focal point, leading to a poor resolution [11]. In contrast, if the material response is enhanced greatly at the focal point and two-photon absorption based polymerization happens only in a small volume within the focal depth (Figure 2(c)), so a very high spatial resolution cab be obtained, which can be even beneath the diffraction limit of the light [12].

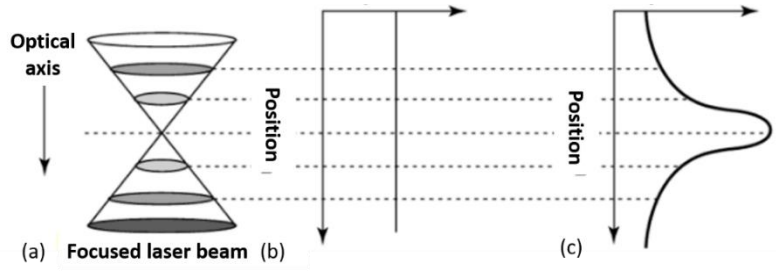

Figure 2. Scheme of TPA and SPA: (a) focused laser beam; (b) total SPA per transversal plane; (c) total TPA per transversal plane. Copyright Polymers for advanced technologies 17, no. 2 (2006): 72-82.

1.1.2. Two-Photon Polymerization Kinetics

To some extent, the principle of TPP is similar to stereolithography, polymerization is usually achieved by the addition of photoinitiators up to a few weight percent (wt%) to absorb at the wavelength of exposure and to promote polymerization, which occurs via opening of chemical bonds (formation of radicals) and subsequent chain reaction [5]. But in a TPP process, the laser beam is focused inside the resin liquid, and the polymerization reaction is a nonlinear process within the focal volume of an ultrashort laser pulse [3-5].

When a high intensity beam is closely focused into the volume of resin, photoinitiator (*PI*) is excited by the simultaneous absorption of two photons and generates free radical fragments ($R\bullet$), which subsequently react with monomers to initiate polymer ($M_1\bullet$) formation. In the propagation step, the growth of the polymer chain occurs by addition of the monomer molecules (M) to the radical center ($M_n\bullet$). The growth of the polymer chain is stopped by primary termination where macroradicals ($M_n\bullet$) react with primary radicals ($R\bullet$) or by bimolecular termination where reaction occurs between two macroradical ($M_n\bullet$) [12]. This procedure can be described as in Figure 3.

Initiation:

$$PI \xrightarrow{h\nu,h\nu} 2R\bullet$$

Propagation:

$$R\bullet + M \rightarrow M_1\bullet$$

$$M_n\bullet + M \rightarrow M_{n+1}\bullet$$

Primary termination:

$$M_n\bullet + R\bullet \rightarrow inactivepolymer$$

Bimolecular termination:

$$M_n\bullet + M_m\bullet \rightarrow inactivepolymer$$

Figure 3. Illustration of Two-Photon Polymerization kinetics

Like any photopolymerization process, TPP is also characterized by steps of initiation, propagation, and termination, but the polymerization kinetics is quite different because of quadratic dependence on applied laser intensity, the threshold effect, and initiation by ultrashort pulsed laser source [13-14]. In order to have a controlled light-material interaction, it is important to understand the nonlinear polymerization kinetics.

1.1.3. The Process of Two-Photon Polymerization

The process of two-photon polymerization is straightforward. A femtosecond laser is tightly focused into a volume of liquid resin, which is mainly composed of monomer and photoinitiator. By means of two-photon absorption, chemical reaction is induced in the optical focus, which brings this liquid resin into a polymerized solid state. These induvial spots shown in Figure 4 are so called voxel, which can be sub-100 nm [15]. When a laser beam is moved around in space under the right irradiation conditions, three dimensional structures can be fabricated by stacking up these voxels. In principle, any complex micro- and nanostructures can be produced by laser scanning in the resin volume without any support.

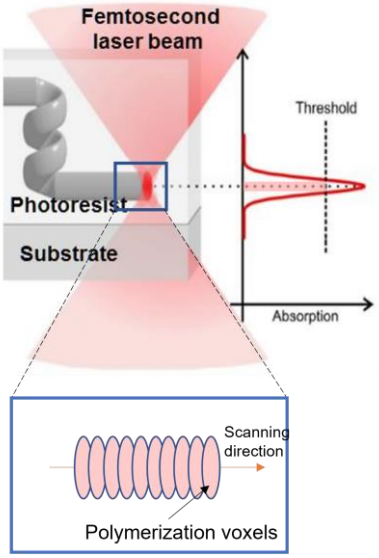

Figure 4. The process of two-photon polymerization

In the end, a process called development is used to a wash out the insufficiently polymerized material with a solvent, and fabricated structures can be obtained. For instance, Figure 5 demonstrates a micro-bull (10-um-long, 7-um-high) with an average voxel size of 120 nm, which is much smaller than the optical focus of 780 nm [15].

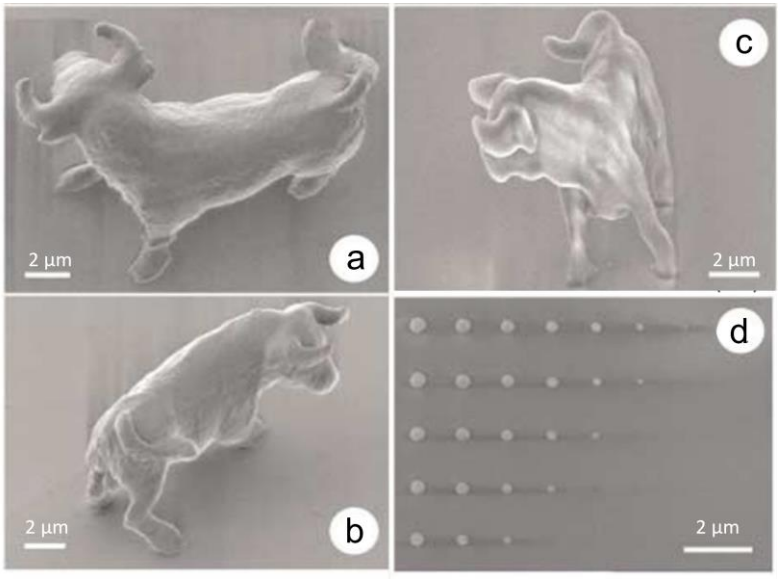

Figure 5. A micro-bull. S. Kawata et al. Nature 412, 697–698 (2001).

1.1.4. Materials for Two-Photon Polymerization

The photomaterials that are used in 3D fabrication by TPP are similar to those employed in conventional lithographic applications. The material consists of two main components: monomer and photoinitiator [16-17]. The monomer will produce the 3D structure, and the photoinitiator will absorb light and provide the active species which initiate the polymerization.

(Meth)acrylate monomers are the principal components of photomaterials because (1) a wide variety of (meth)acrylates ranging in molecular weights, structural moieties, and degree of functionality are commercially available, (2) they are transparent at visible and NIR wavelengths, resulting in no absorption of light linearly at these wavelengths, (3) they can be generally polymerized at rapid rate of propagation with an efficient termination in the presence of oxygen, which allows excellent spatial and temporal control of the polymerization process [17-18]. Some common and commercially available acrylate monomers are shown in Figure 6.

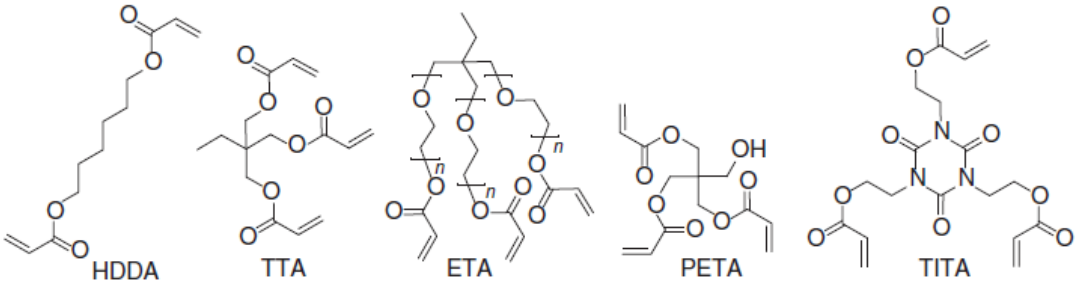

Figure 6. Common acrylate monomers. Copyright ACS Applied Polymer Materials 1, no. 4 (2019): 593-611.

Free radical photoinitiators can be classified into Norish type I and II initiators, the research employed a Norish type I photoinitiator: 2,2-Dimethoxy-2- phenylacetophenone (Irgacure 651), which generates radical pairs through a highly efficient α-cleavage process [19-20]. Both of the radical pairs react with (meth)acrylate monomers, initiating the polymerization of monomers.

Aside from acrylate monomers, epoxy based cationic resin are solid photoresponsive materials that undergo ring opening polymerization [17]. Since the research employed pentaerythritol tetraacrylate (PETA) as the functional acrylate monomer, epoxy based cationic resin will not be discussed in the dissertation.

1.1.5. Applications of Two-Photon Polymerization

Nowadays, TPP has been broadly applied. Examples are demonstrated in Figure 7. Figure 7(a) is an image of a foam material where the density of the material changes by a factor of seven within about 100-micron thickness and these types of materials are very useful in controlling the temporal shape of the pressure wave [21]. Figure 7(b) shows micro needle valves, used to regulate the flow of blood, two-photon polymerization is employed with a fine nanoscale resolution to make sure that the surfaces are smooth [22]. Figure 7(c) shows polymeric micro lattices with strut lengths of the order of 5–10 μm and strut diameters down to 1 μm. The strength of the lightweight mechanical metamaterials approaches the theoretical limit because of the fine resolution with TPP [23]. Figure 7(d) is a 3D printed objective lens on optical fibers with sizes around 100 μm, it consists of five refractive surfaces for imaging and is directly fabricated on the optical fiber (red) [24].

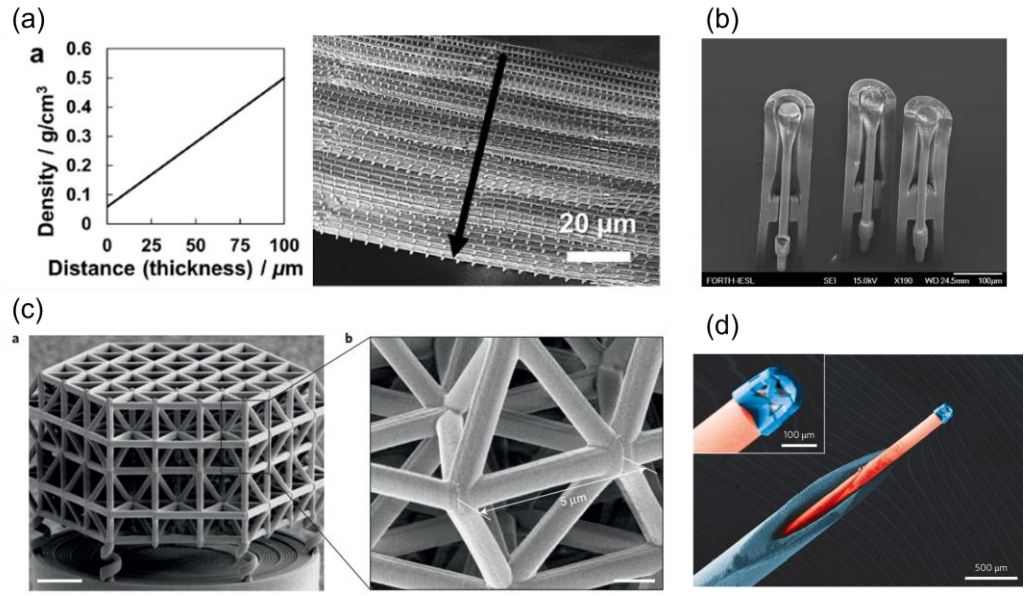

Figure 7. Applications of two-photon polymerization. Copyright Oakdale et al., Adv. Funct. Mater., 2017; Bauer et al., Nature Materials, 2016; Farsari et al., Nature Photonics, 2009; Gissibl et al., Nature Photonics, 2016.

1.2. Ways to Improve Two-Photon Polymerization Fabrication Throughput

1.2.1. Slow Fabrication of Conventional TPP

The difference about the two-photon polymerization process versus other photopolymerization based additive manufacturing is the sub diffraction feature size. Despite the sub diffraction feature size, so far TPP is largely considered as a slow fabrication method. This is because in most cases the laser beam is focused into a Gaussian spot in space, which limits how fast the laser beam can cover a large area or volume. For example, it takes about 45 minutes to fabricate a photonic crystal in a diameter of 40 um (Figure 8(a)), which means a scaled up functional device as small as 1 mm in diameter will take more 400 hours [25]. Another example is the scaffold (Figure 8(b)) for cell growth, which is a 1-millimeter structure, the fabrication time is about 60 hours. So, there is a tradeoff between resolution and fabrication speed. The challenge is to break this trade-off, speed up the printing process while maintaining the superb sub-wavelength feature size.

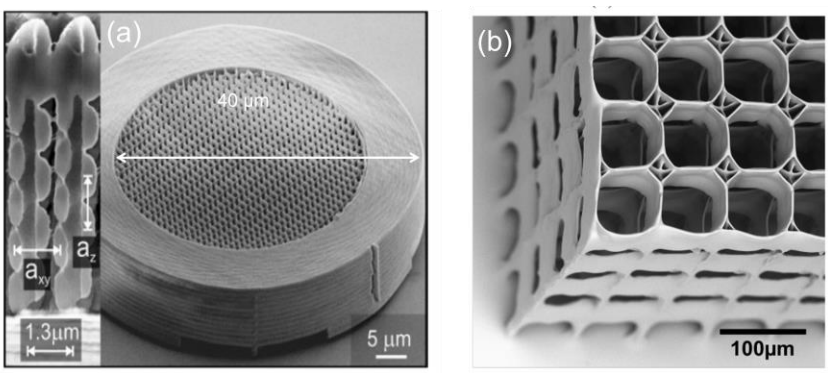

Figure 8. (a) 3D spiral photonic crystals fabricated by TPP. M. Thiel et al. Adv. Mater. 19, 207–210 (2007); (b) Scaffolds fabricated by TPP . Trautmann, A., et al. Optics express 26.23 (2018): 29659-29668

1.2.2. Parallel Laser Writing

There are a couple of ways to do that. Parallel laser writing is one way to speed up fabrication, a spatial light modulator (SLM) is used to create multiple focal spots in the liquid resin to multiply the writing speed during point scanning [26]. As shown in Figure 9(c), different colors represent voxels exposed by foci of different holographic beams, thus enabling the parallel fabrication of multiple microstructures.

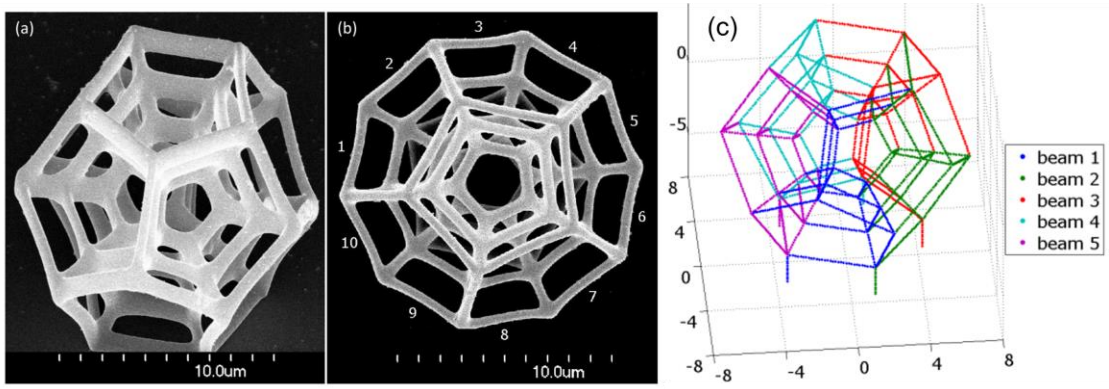

Figure 9. Scanning electron microscope images of a holographically polymerized test structure, with viewing angle 45◦ (a) and top view (b), (c) Three-dimensional plot of the test microstructure voxel coordinates. Different colors show voxels exposed by foci of different holographic beams. G. Vizsnyiczai et al. Opt. Express 22, 24217 (2014)

1.2.3. Projection-Based TPP

Projection-based TPP is another way. A thin 2D layer is printed by projecting a patterned mask that was focused inside the liquid resin. 3D structures are fabricated using a layer-by-layer printing method [27]. As shown in Figure 10, a pre-stretched ultrashort pulse is progressively shortened as it travels through the liquid resin so that the shortest pulse that has the highest light intensity is achieved only at the spatial focal plane. So, there is no polymerization above or below the focal plane.

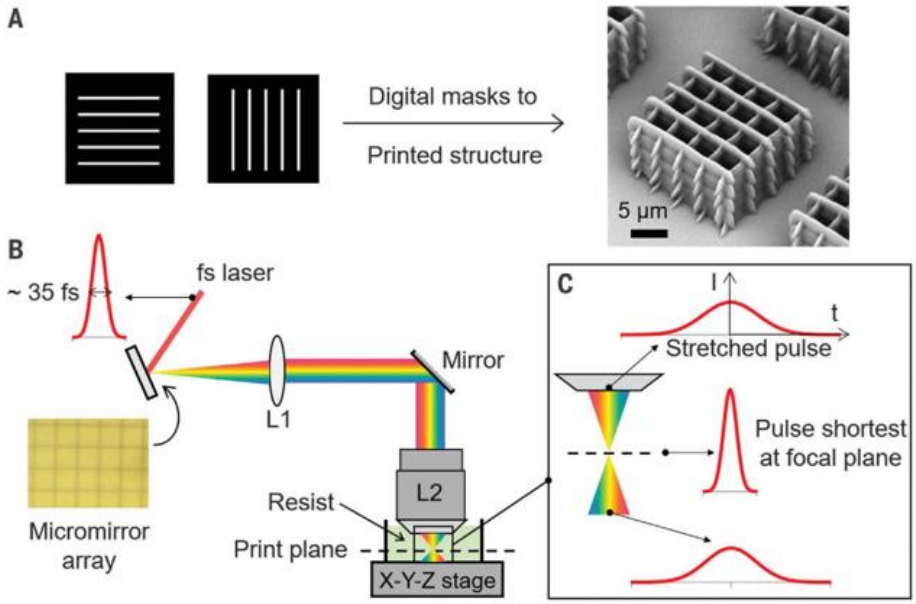

Figure 10. Experimental setup of projection based TPP. Copyright. Science 366, 105–109 (2019).

1.2.4. Beam Wavefront Engineering

This work focuses on another method, called beam wavefront engineering. The helix array on the left (Figure 11) was fabricated by a twisting beam as shown in here. The beam is generated by encoding information ("phase mask") to a Gaussian beam by a spatial light modulator [28]. The

scaffold structure on the right is fabricated by a zeroth order Bessel beam, which is engineered by focusing a Gaussian beam with an axicon lens.

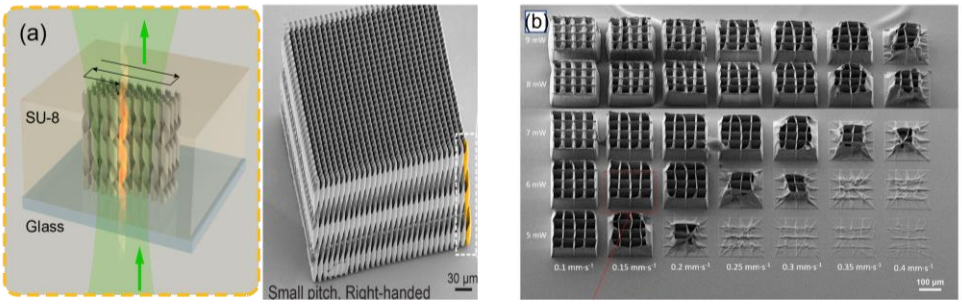

Figure 11. (a) Fabrication of a helix array using a twisting beam; (b) A scaffold structure fabricated by a zeroth order Bessel beam. Copyright Photonics Research 10, 303 (2022). Applied optics, 58(13), pp.D91-D97

As shown in Figure 12, Bessel beam has a non-diffractive focus, and its depth of field is significantly longer than the Rayleigh range of a Gaussian beam of a comparable diameter. The result is Bessel beam can be used to fabricate high-aspect-ratio structures, and large-volume fabrication can be achieved by laser beam engineering.

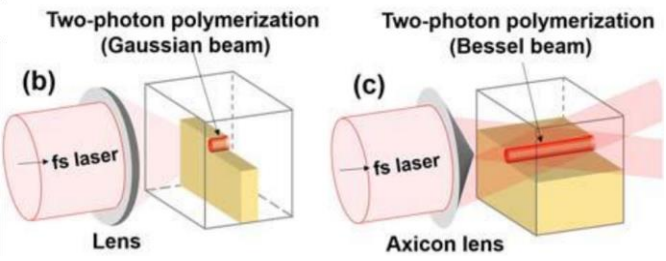

Figure 12. The comparison between Gaussian beam and Bessel beam

Chapter 2 - Mathematical Model Development of the Two-Photon Polymerization Process

2.1. Spatial Laser Beam

Gaussian beam is the most common beam shape currently used in ultrafast laser material processing because of its ability to radiate into a small focused spot and print arbitrarily complex 3D micro- and nanostructures point by point [29]. The Gaussian beam is a radially symmetrical distribution whose electric field is given by the following equation:

$$E(r,z) \propto \exp\left(-\frac{r^2}{\omega(z)^2}\right)\exp[i\varphi(z,r)] \tag{1}$$

$$r = \left(x^2 + y^2\right)^{\frac{1}{2}} \tag{2}$$

Where, r is defined as the distance from the beam axis, z is the coordinate along the propagation direction, $\omega(z)$ is the Gaussian beam radius, and $\varphi(z, r)$ is a term describing the phase evolution along the beam as well as the curvature of the wave fronts:

$$\varphi(z,r) = kz - \arctan\frac{z}{z_R} + \frac{kr^2}{2R(z)} \tag{3}$$

$$z_R = \frac{\pi\omega_0^2}{\lambda} \tag{4}$$

Here, $k = 2n/\lambda$ is the wave number, $R(z)$ is the curvature of the wave fronts, and Z_R is the Rayleigh length calculated from the beam radius ω_0 at the beam focus.

The variation of the beam spot size $\omega(z)$ and the beam intensity $I(r,z)$ are given by Equation (5) and Equation (6), respectively [30]:

$$\omega(z) = \omega_0\sqrt{1+\left(\frac{z}{z_R}\right)^2} \tag{5}$$

$$I(r,z) = I_0\left(\frac{\omega_0}{\omega(z)}\right)^2 \exp\left(\frac{-2r^2}{\omega^2(z)}\right) \tag{6}$$

where I_0 is the laser intensity at the center of the Gaussian beam and ω_0 is the theoretical beam radius.

A Gaussian beam of wavelength 515 nm, peak intensity 5×10^{16} W/m^2, and waist diameter 1.76 um was employed in the study, the laser profile is as shown in Figure 13.

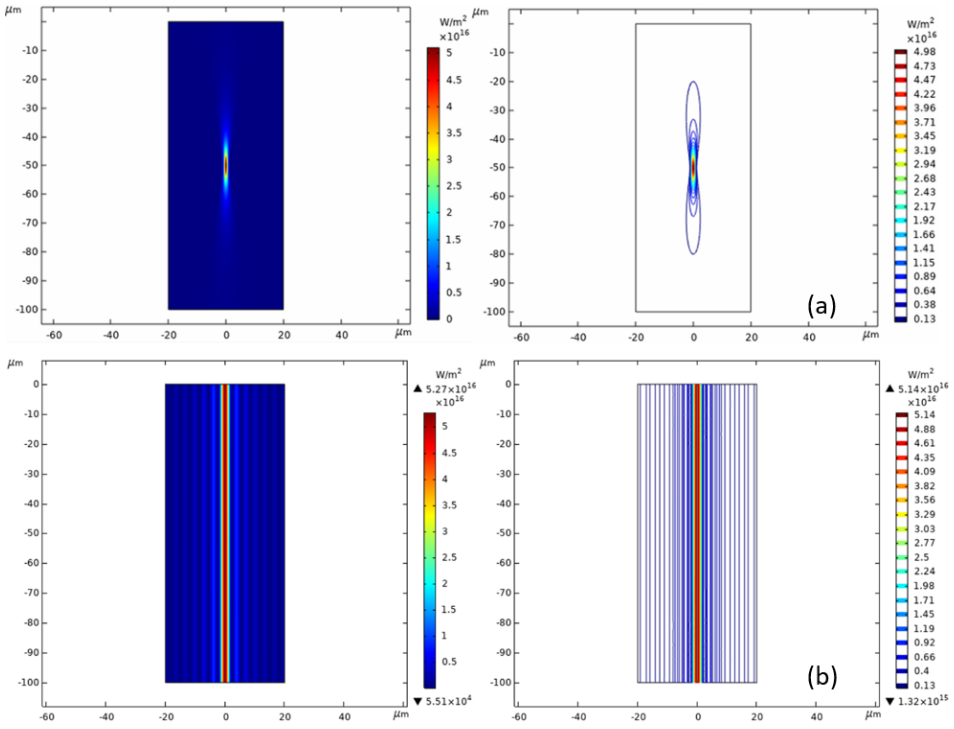

Figure 13. The laser profile of (a) Gaussian beam and (b) Bessel beam

The employment of Gaussian beam in TPP has been challenged by the short Rayleigh range. To overcome the limitation, an application of non-diffractive Bessel beam for photopolymerization has been attempted recently because Bessel beam can achieve the depth of field significantly longer than the Rayleigh range of a Gaussian beam with a comparable diameter. This characteristic makes Bessel beam suitable for fabrication of high aspect ratio structures [31].

The ideal *zero*-th order Bessel beams constitute a class of solutions to the Helmholtz wave equation with rotational symmetry and are invariant along the propagation direction. Such idealized non-diffractive beams have infinite transverse extent and carry infinite amount of energy and, therefore, cannot be realized experimentally. However, over a limited spatial range, an approximation to such idealized beams can be obtained by using Gaussian beams and can be described by [32]:

$$I(r,z) = 2\pi k\left(\tan^2\alpha\right)(n-1)^2 z I_0 e^{-2\left((n-1)z\tan\alpha/\omega_0\right)} J_0^2\left(k(n-1)r\tan\alpha\right) \tag{7}$$

$$k = \frac{2\pi}{\lambda} \tag{8}$$

Where r and z are the radial and longitudinal coordinates respectively; I_0 is the incident on-axis intensity, ω_0 is the incident beam waist, n is the glass refractive index. J_0 is the *zero*-th order Bessel function. The laser profile of Bessel beam is as shown in Figure 13(b).

2.2. Species Concentration Distribution

The photopolymerization process consists of three basic types of chemical reactions: initiation, propagation, and termination. Light irradiation causes the destruction or excitement of the photoinitiator leading to the generation free radicals. The addition of free radicals to the first monomer molecule to produce the chain-initiating radical $M_1\bullet$. Propagation consists of the growth of $M_1\bullet$ by the successive additions of many monomer molecules, which allows for the growth of linear macromolecules. At some point, the propagating polymer chain stops growing and terminates. Termination occurs by bimolecular reaction between radicals, where two radicals react with each other by combination.

The spatial and temporal change in the photoinitiator concentration (PI) on laser irradiation is presented by Equation (9) [6-7]. The first term on the right side represents the

diffusion of photoinitiator molecules. In a TPP process, the decomposition of the photoinitiator depends on the square of applied photon flux ϕ, which is represented by the second term on right side.

$$\frac{\partial PI}{\partial t} = d_{PI} \cdot \left(\frac{\partial^2}{\partial x^2} + \frac{\partial^2}{\partial y^2} + \frac{\partial^2}{\partial z^2} \right) PI - \psi \cdot \delta \cdot \phi^2 \cdot PI \tag{9}$$

$$\phi = \frac{I}{h\nu} \tag{10}$$

Where d_{PI} is the molecular diffusion constant that varies both spatially and temporally due to temperature distribution, ψ represents the quantum yield of the photoinitiator, δ is the two-photon absorption cross section of the photoinitiator, representing the ability of photoinitiator molecules to transit from the ground state to the excited state, I is the laser intensity distribution in radical and axial directions; h is Plank's constant, and ν is the laser frequency.

Free radicals (R) are generated by the decomposition of photoinitiator molecules, and their concentration varies both spatially and temporally as it depends on various kinetic and transport processes. It is also important to consider the factors that may lead to radical termination, including radical combination and oxygen quenching. Radical combination relates to the reaction between active radicals that render them useless. Oxygen quenching is due to the presence of oxygen molecules that combine with primary radicals and convert them into species that are unable to initiate propagation. The concentration of oxygen present in the photomaterials can change the threshold for polymerization as the polymerization reaction will not propagate until the oxygen molecules are significantly reduced.

Apart from radical generation and termination, the radicals also diffuse spatially. Equation (11) describes the radical dynamics, the first term on the right side represents radical

diffusion, the second term represents radical generation on photoinitiator decomposition, and the last two terms represent radical termination kinetics, attributing to radical combination and oxygen quenching, respectively [6,7,33].

$$\frac{\partial R}{\partial t} = d_R \cdot \left(\frac{\partial^2}{\partial x^2} + \frac{\partial^2}{\partial y^2} + \frac{\partial^2}{\partial z^2} \right) \cdot R + \psi \cdot \delta \cdot \phi^2 \cdot PI - 2k_t \cdot R^2 - k_q \cdot OX \cdot R \tag{11}$$

Here, d_R is the radical diffusion constant that varies both spatially and temporally due to temperature distribution; k_t and k_q are termination and oxygen quenching constants, respectively; OX represents the concentration of oxygen molecules.

The propagation reaction consists of the combination of radical with monomer molecules *M*, which changes the monomer concentration as the monomer converts into a high molecular weight polymer as presented by Equation (12) [6,7]:

$$\frac{\partial M}{\partial t} = d_M \cdot \left(\frac{\partial^2}{\partial x^2} + \frac{\partial^2}{\partial y^2} + \frac{\partial^2}{\partial z^2} \right) \cdot M - k_p \cdot R \cdot M \tag{12}$$

The first term on the right side in Equation (12) represents the diffusion of monomer molecules caused by the spatial gradients in monomer concentration. The second term stands for the effect of monomer propagation reaction, where k_p is the propagation constant.

The concentration of oxygen present in the photomaterials can change the threshold for polymerization as the polymerization reaction will not occur until the oxygen molecules are significantly reduced. Hence, the concentration of oxygen changes as the reaction progresses and is defined by Equation (13) [6,7,33]:

$$\frac{\partial OX}{\partial t} = d_{OX} \cdot \left(\frac{\partial^2}{\partial x^2} + \frac{\partial^2}{\partial y^2} + \frac{\partial^2}{\partial z^2} \right) \cdot OX - k_q \cdot R \cdot OX \tag{13}$$

The first term on the right side in Equation (13) represents the diffusion of oxygen molecules. The second term stands for the reaction of oxygen quenching, where k_q is the quenching constant.

It should be noted that, species diffusion constants d_{PI}, d_R, d_M have an Arrhenius relationship with temperature as shown in Equation (14), where d_{j0} are pre-exponential factors, R is the gas constant, E_a is the activation energy for diffusion. The diffusion constant of oxygen d_{OX} is considered as temperature independent.

$$d = d_{j0} \exp\left(\frac{-E_a}{R[T]}\right)\left(j = PI, R, M\right) \tag{14}$$

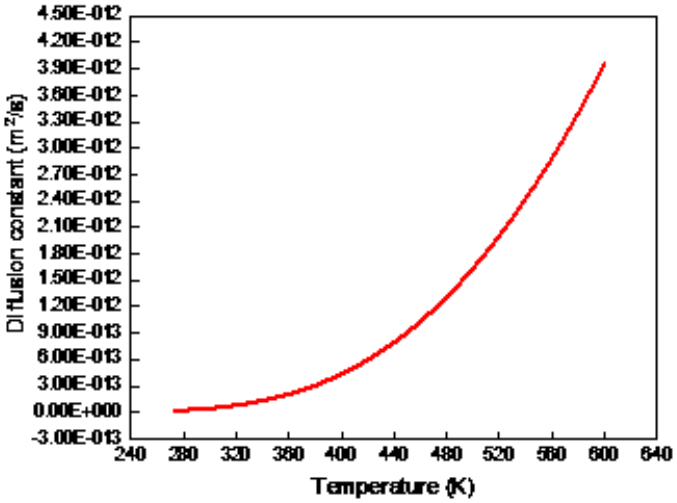

Figure 14. The dependence of species (photoinitiator, radical, and monomer) diffusion constant on temperature

Propagation and termination constants (k_p and k_t) have an Arrhenius relationship with temperature and experimentally extrapolated dependence on monomer conversion (c) as shown in Equation (15) and (16), respectively.

$$k_p = k_{p0} \cdot \exp\left(\frac{-E_{pa}}{R \cdot T}\right) \cdot 10^{-(5.115 \cdot c^2 + 0.472 \cdot c)} \tag{15}$$

$$k_t = k_{t0} \cdot \exp\left(\frac{-E_{pa}}{R \cdot T}\right) \cdot 10^{-(3.892 \cdot c^2 + 1.9538 \cdot c)} \tag{16}$$

where k_{p0} and k_{t0} are pre-exponential factors, E_{pa} and E_{ta} are activation energy for molecules of monomer and radical, and c = 1-M/M_0 is defined as monomer conversion.

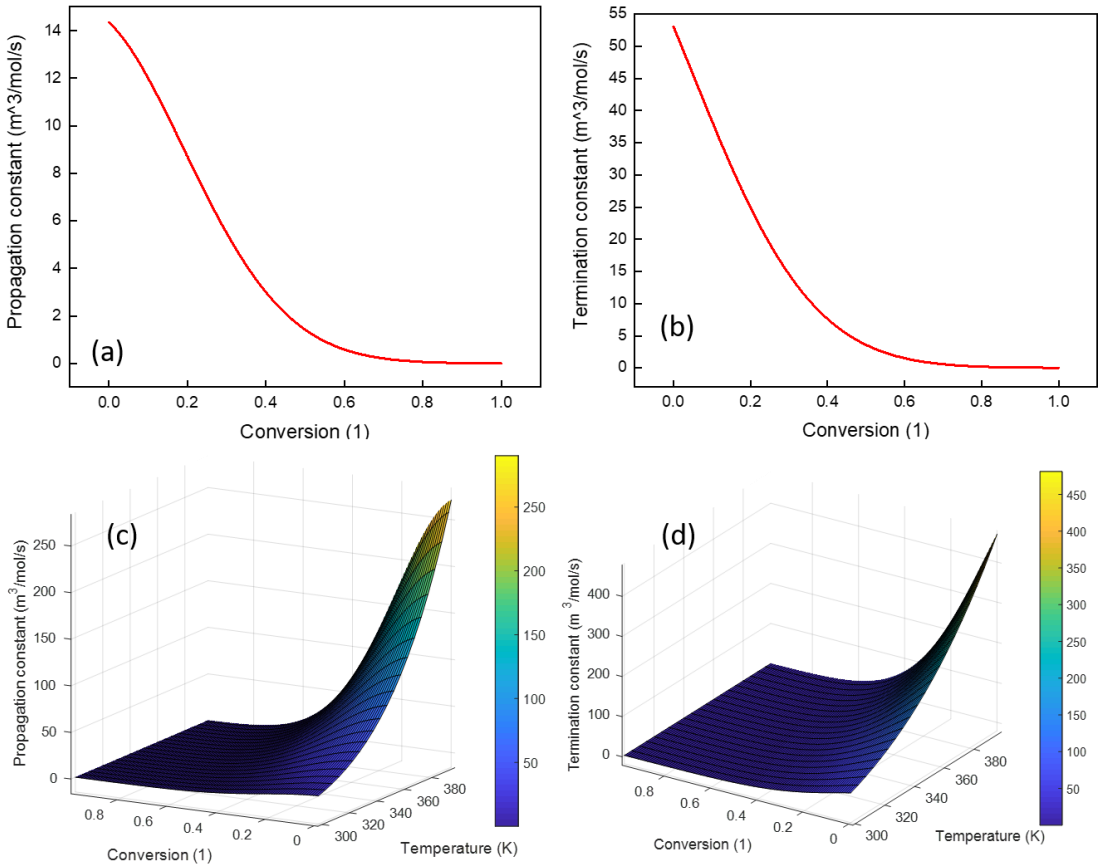

Figure 15. (a) Dependence of propagation constant on monomer conversion at room temperature; (b) Dependence of termination constant on monomer conversion at room temperature; (c) Propagation constant over monomer conversion and temperature; (d) Termination constant over monomer conversion and temperature

2.3. Temperature Distribution

During the TPP printing process, the temperature of the irradiated structure increases due to the laser absorption and the exothermic chemical reaction. A spatial-temporal temperature distribution inside the laser-drawn acrylates structure can be solved by following the partial differential equation (17) [6,7,33]:

$$\rho C \frac{\partial T}{\partial t} = k \cdot \left(\frac{\partial^2}{\partial x^2} + \frac{\partial^2}{\partial y^2} + \frac{\partial^2}{\partial z^2} \right) \cdot T - H \frac{\partial M}{\partial t} + c \cdot \alpha \cdot I \tag{17}$$

$$c = 1 - \frac{M}{M_0} \tag{18}$$

Where ρ is the density of photomaterials, C is specific heat capacity, T is the temperature, k is the heat conductivity, H is the enthalpy change of the polymerization, c is monomer conversion, and α is the molar extinction coefficient of the monomer. The first term on the right side describes standard heat conduction, the second term depicts the exothermic heat generation, and the last term accounts for the heat generation by laser absorption.

The photomaterial was loaded between two microscope slides separated by a spacer having a thickness of ~200 μm. The sample cell was positioned within the focus of laser beam.

A convection thermal boundary condition can be made between glass slide and air, and an interface thermal boundary condition is set between photomaterial and microscope slides.

$$-k_{glass} \frac{\partial T_{glass}}{\partial x} = -k_{resin} \frac{\partial T_{resin}}{\partial x} \tag{19}$$

$$k_{glass} \frac{\partial T}{\partial x} = h\left(T - T_{\infty}\right) \tag{20}$$

2.4. Numerical Methods

The finite element method (FEM) for modeling TPP was implemented in COMSOL Multiphysics. This model employs a fixed (Eulerian) discretized mesh spanning the domain as shown in Figure 16. Finer meshes are applied to the laser irradiated region, and coarser meshes are used in the other areas which are of less interest.

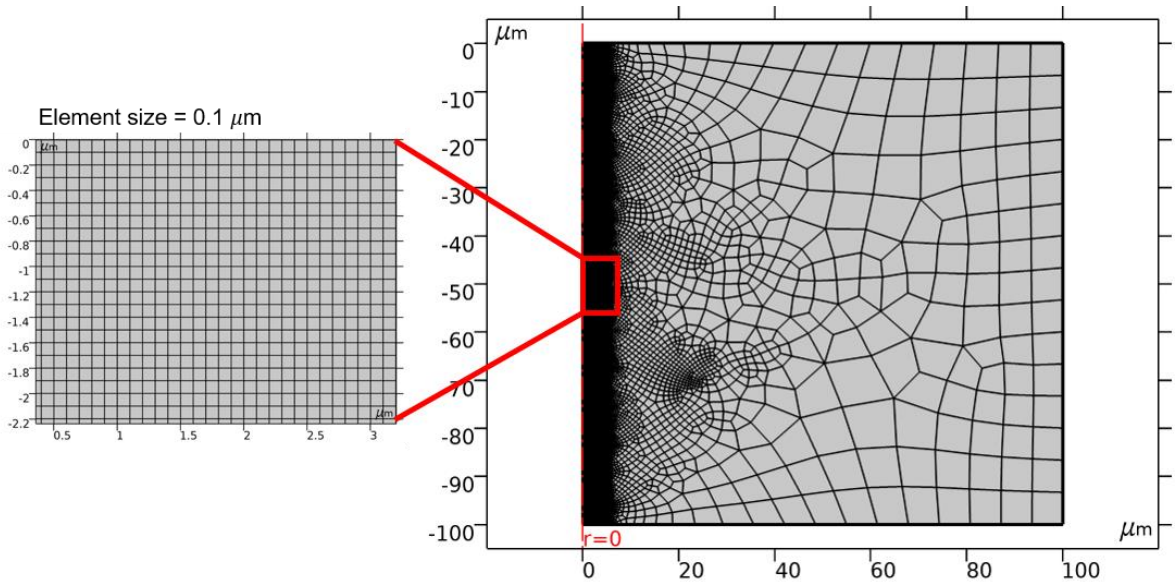

Figure 16. A customized mesh, which contains more mesh elements around the irradiated volume

The selection of mesh size is important. The mesh must be able to achieve accurate results while balancing between element size and computation time. To determine the optimal element size, a mesh convergence analysis was performed under the conditions of 1 kHz and 6 μJ. As demonstrated in Figure 17, when the element size is smaller or equal to 0.1 μm, the computed results (*PI* and *R* concentration) converge to a repeatable solution with decreasing element size. So, the element size of 0.1 μm is applied to the laser irradiation region as additional refinement is unnecessary after reaching mesh independence.

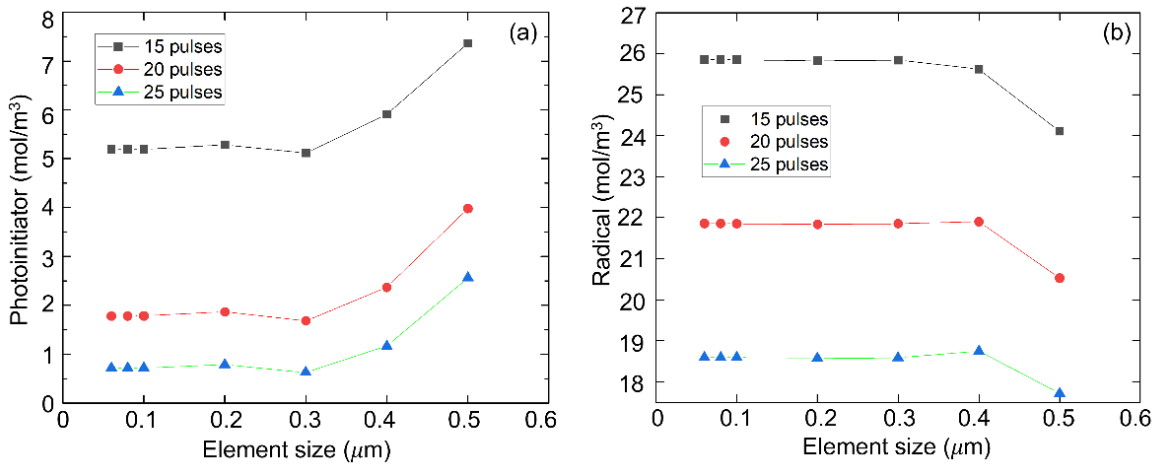

Figure 17. Results from an analysis of mesh-convergence

In addition to the mesh size, the time-stepping algorithm plays an important role in the fidelity and efficiency of computation. An implicit time-stepping algorithm installed in COMSOL Multiphysics was used to solve the time-dependent problem. The algorithm chooses a time step based upon a user-specified relative tolerance. Loose tolerance can skip over certain transient events, while tight tolerance might take up too much computational resource. To accurately and efficiently model femtosecond laser irradiation with pulse duration on the order of 170 fs, an *Events Interface* in COMSOL Multiphysics was used to force a solution evaluation when the pulse switches on at a known laser frequency. So, small time steps are taken immediately after the events to give good resolution of the variation, and large time steps are taken when the laser irradiation is off to minimize the overall computational cost.

The Backward Differentiation Formula (BDF) is implemented to solve the ordinary differential equations. Table 1 lists the process and material parameters for two-photon polymerization. The simulated results are presented and discussed in the following chapters.

Table 1. Process and material parameters for two-photon polymerization

Parameter	**Description**	**Value**	**Reference**
τ	Pulse duration	170 *fs*	Experiment

f_{rep}	Repetition rate	1 *kHz/* 80 *MHz*	Experiment
λ	Wavelength	515 *nm*	Experiment
ω_0	Beam radius	0.88 *um*	Experiment
δ	Two-photon cross section (Irgacure 819)	*5 GM*	[34]
ψ	Quantum yield	0.42	[35]
I_0	Peak intensity	5.22×10^{16} W/m^2	Experiment
d_{j0} ($j = PI,R,M$)	Pre-exponential diffusion constant	3.26×10^{-10} m^2/s	[36]
d_{OX}	Diffusion constant for oxygen	2.27×10^{-10} m^2/s	[36]
k_{p0}	Pre-exponential propagation constant	2.4×10^{6} $m^3/mol/s$	[36]
k_{t0}	Pre-exponential termination constant	3.59×10^{5} $m^3/mol/s$	[36]
k_q	Quenching constant	2.3×10^{3} $m^2/mol/s$	[36]
E_{pa}	Propagation activation constant	30000 *J/mol*	[37]
E_{ta}	Termination activation constant	22000 *J/mol*	[37]
E_a	Diffusion activation constant	22000 *J/mol*	[37]
M_0	Monomer concentration	11868 mol/m^3	Experiment
PI_0	Photoinitiator concentration	132 mol/m^3	Experiment
OX_0	Oxygen concentration	6 mol/m^3	Experiment
ρ	Resin density	1190 kg/m^3	[38]
C	Resin heat capacity	1870 *J/kg/K*	[38]
k	Resin thermal conductivity	0.142 *W/m/K*	[38]
H	Enthalpy of polymerization	-54800 *J/mol*	[36]
α	Molar absorption coefficient for the polymer	11.5 m^{-1}	Experiment

Chapter 3 - Model Validation

The experimental setup to validate the model has been described previously [28]. The laser source is a femtosecond laser (Pharos, Light Conversion, Lithuania) delivering 170 fs laser pulses at a wavelength of 1030 nm. The laser beam then passes a second harmonic generation module, and the 515 nm laser beam is used for TPP. The 515 nm laser beam is focused by an axicon (Doric Lenses Inc., Canada) with a base angle of 25° to create a Bessel beam with a narrow center lobe (< 2 μm in diameter) and a long depth of focus (> 10 mm).

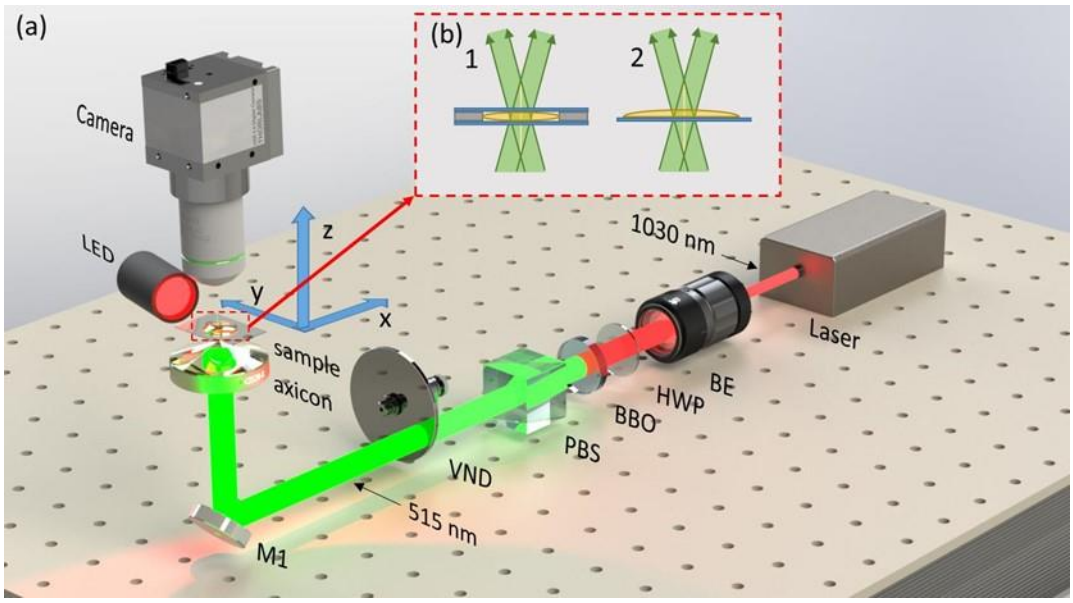

Figure 18. Experimental setup at CREOL, The College of Optics and Photonics at University of Central Florida. Copyright Applied optics, 58(13), pp.D91-D97

To verify the model predictions, experiments were conducted at the University of Central Florida by Dr. Xiaoming Yu's group. High aspect ratio pillar structures were fabricated using the Bessel beam with P = 5 mW - 22 mW and pulse numbers of 20 - 50 pulses at 1 kHz repetition rate in a commercial acrylic resin (3D ink, USA). After laser exposure, polymerized structures were rinsed with isopropyl alcohol to remove uncured resin and then dried. Developed pillar structures were examined with SEM (Ultra 55 FEG, Carl Zeiss AG, Germany) for imaging and

measurement. The predicted size of a polymerized structure was determined by the polymerization threshold line (60%) as illustrated in Figure 19.

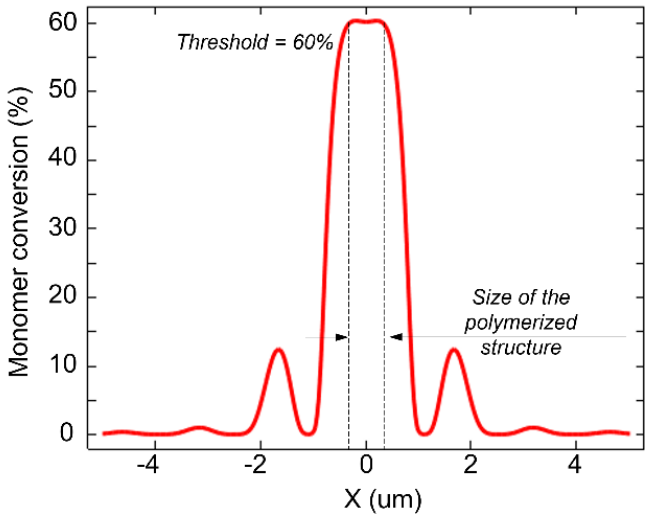

Figure 19. Predicted size of a polymerized feature assuming polymerization threshold is 60% monomer-conversion.

Figure 20 shows the comparison between SEM-measured and model-predicted polymerized pillar structure diameters. In general, measured pillar diameters increase with *P*, although there are some fluctuations observed at high laser power due to experimental variance. The simulation, entirely driven by parameters adopted from the literature [13,29-34], manage to estimate pillar structure diameters that are comparable, within one order of magnitude, to the experimental measurements.

The stepwise behavior of the diameter growth presented in the predictions in Figure 20 is caused by the polymerization of Bessel beam side lobes. The first, second, and third side lobes are 16%, 9%, and 6% of the peak intensity of the central lobe. These side lobes can also polymerize the photocurable resin during TPP once exceeding the polymerization threshold (60%). For instance, at the end of 50th pulse (Figure 20(d)), the predicted diameter gradually grows from 1.33 μm to 1.65 μm as *P* increases from 5 mW to 8 mW, then the diameter abruptly

jumps to 3.78 μm when the P increases to 10 mW. This phenomenon is attributed to the polymerization caused by the first side lobe. The second jump of diameter occurs at P = 18 mW due to the polymerization caused by the second side lobe of the Bessel beam. Similar observations are also found in experimental measurements highlighted in Figure 20(d).

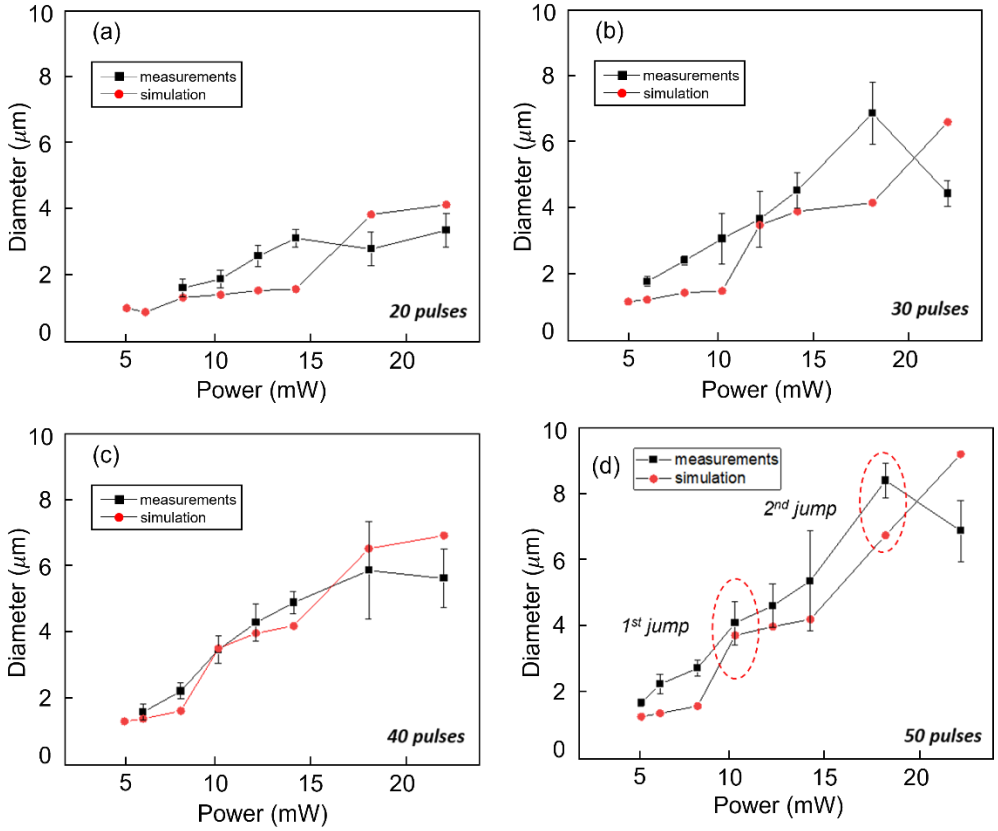

Figure 20. Comparison of pillar-diameters determined from experiment and simulation versus average input power P for various numbers of total pulses. Measured data were provided by Dr. Xiaoming Yu's group [28].

Chapter 4 - Results and Discussion

4.1. Evolution of Species and Temperature in TPP at 1 kHz

4.1.1. The Evolution of Photoinitiator Concentration

Figure 21(a) depicts the temporal change of the concentration of photoinitiator at the center of the Bessel beam irradiation. Given that the Bessel beam is non-diffractive, the species concentration along the direction of beam propagation (z) is assumed to be constant. The photoinitiator concentration decreases with each laser pulse and remains almost unchanged during the dark period because diffusion of the photoinitiator is negligibly small. The reduced photoinitiator concentration at the end of each dark period becomes the initial condition for the next pulse, which affects the amount of radicals generated and eventually the polymerization kinetics. Overall, the photoinitiator concentration decays at a rate that depends on the square of the peak-intensity I_0 and follows the envelope of $\exp(-\psi\delta\tau_{\exp}(I_0/h\nu)^2)$. Here, $\tau_{exp} = N/f$ is the total time elapsed after exposure with N pulses. Figure 21(b) demonstrates that the spatial distribution of the photoinitiator correlates with the beam intensity profile. For instance, the photoinitiator is depleted rapidly at the center lobe of the Bessel beam ($x = 0$), where the laser intensity is the highest. No photoinitiation occurs in the valleys between concentric rings of the Bessel beam where the intensity is zero.

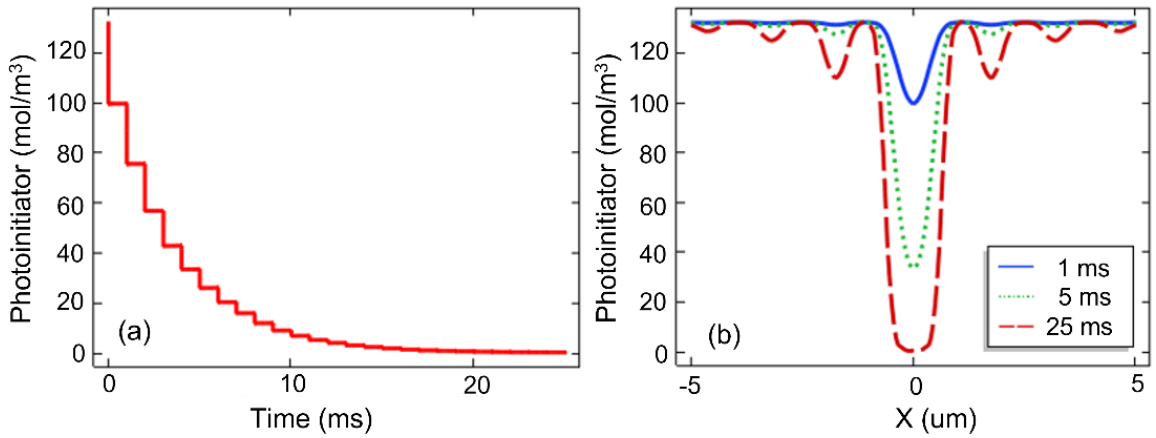

Figure 21. The temporal evolution of photoinitiator concentration (f = 1 kHz, E_p = 6 μJ) at the center of the Bessel beam (x = 0). (b) The photoinitiator concentration along the radial direction at three times after start of the exposure.

4.1.2. The Evolution of Radical Concentration

The temporal and spatial distributions of radicals define the volume where polymerization takes place. Figure 22(a) demonstrates that the concentration of radicals at the center of the Bessel beam increases with decomposition of the photoinitiator by laser irradiation. The generated radicals decay rapidly till the next pulse arrives due to *R-R* recombination and quenching by oxygen. Polymerization does occur during this period but does not change the concentration of radicals because addition of monomer merely propagates the radical. Figure 22(b) shows the spatial distribution of radical concentration. At the end of 1 ms and 5 ms, the maximum radical concentration appears at the center of the focal volume because of high laser intensity and the accumulation of radicals. In contrast, a double-peaked curve is observed at the end of 25 ms, implying that radical concentration at the center of Beam drops compared to the immediate vicinity where the intensity is lower. This change is caused by *R-R* termination, which is strongest at the center of the beam where the laser intensity is highest. In this region, the radical concentration drops rapidly during the dark period, whereas areas with lower radical

concentration do not experience significant *R*-*R* recombination. This phenomenon indicates that high laser intensities could lead to the inefficient utilization of radicals.

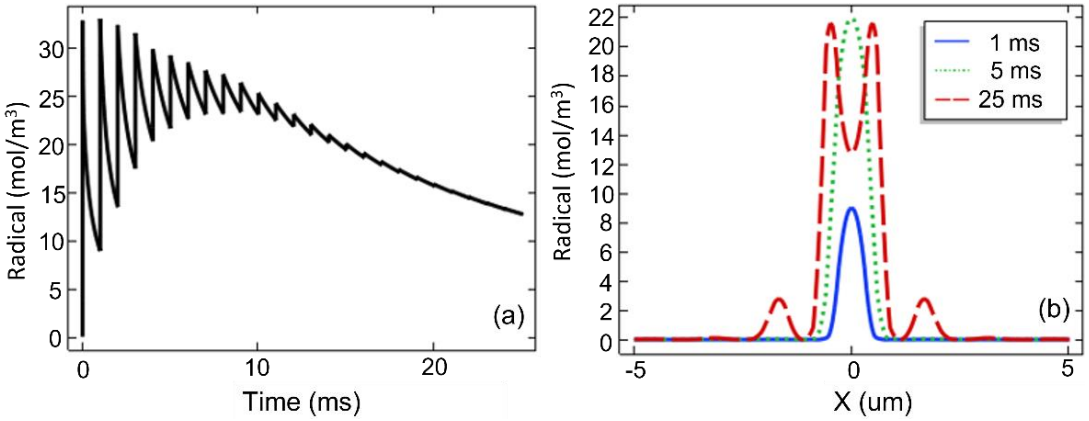

Figure 22. The temporal evolution of radical concentration (f = 1 kHz, E_p = 6 μJ) at the center of the Bessel beam (x = 0). (b) Radical concentration along the radial direction at three times after start of the exposure.

4.1.3. The Evolution of Oxygen Concentration

Figure 23(a) shows that oxygen is rapidly depleted around the focal region due to rapid quenching and diffusion. Radicals generated by the first pulse consume all oxygen inhibitors, enabling polymerization to begin. Oxygen molecules are then replenished by diffusion into the irradiated volume. As shown in Figure 23(b), the oxygen depleted region broadens with subsequent pulses. The most severe oxygen depletion occurs at the center lobe, whereas the oxygen is only partially consumed in the vicinity. Diffusion drives oxygen from the surroundings into the irradiated volume and decreases the concentration gradient.

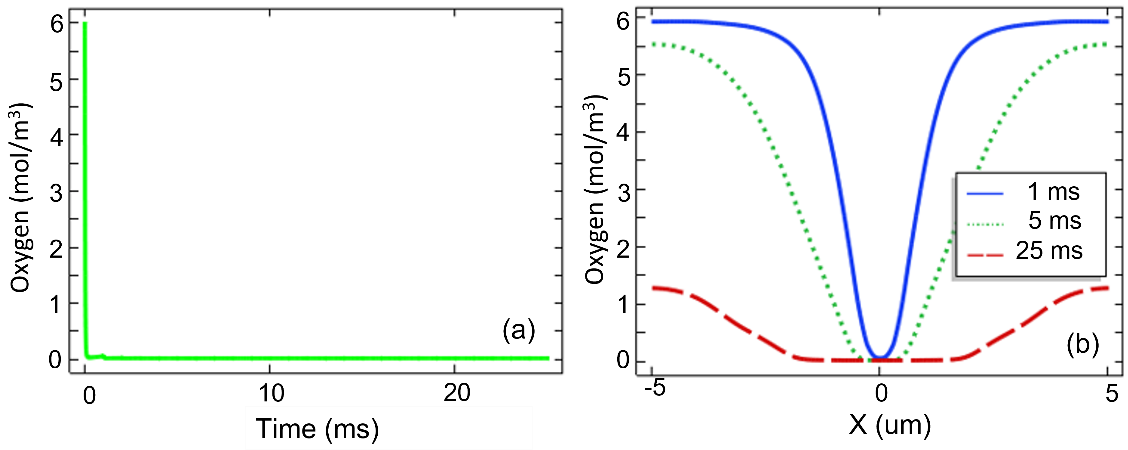

Figure 23. (a) The temporal evolution of oxygen concentration (f = 1 kHz, E_p = 6 μJ) at the center of the Bessel beam (x = 0). (b) Oxygen concentration along the radial direction at three times after start of the exposure.

4.1.4. The Evolution of Monomer Concentration

Figure 24(a) shows the temporal profile of monomer concentration and %-conversion to polymer. The rate of monomer consumption is high at first, but it decreases with each pulse. The shape of the polymerized voxel is defined by the area that exceeds a critical conversion threshold value. In these simulations, the threshold was taken to be 60%. The threshold value was determined by Raman spectroscopy of polymerized features that were sufficiently robust to withstand the developing process. The contour obtained from the monomer conversion plot (Figure 24(b)) can be used to predict the dimension of a polymerized structure, based on which the model can be compared to experimental results.

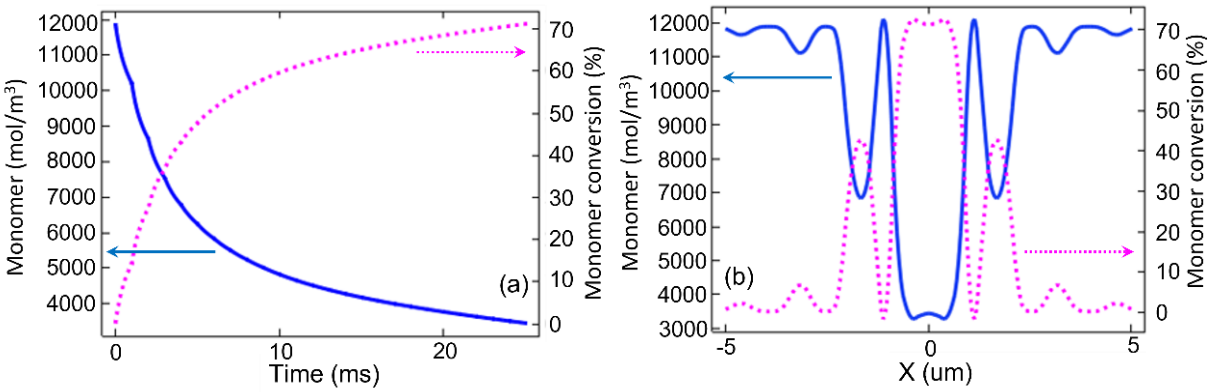

Figure 24. (a) The temporal evolution of monomer concentration/conversion (f = 1 kHz, E_p = 6 μJ). (b) The monomer concentration/conversion along the radial direction.

4.1.5. The Evolution of Temperature Distribution

Figure 25 is a double Y-axis plot. The left axis gives temperature, which increases due to exothermic polymerization and absorption of laser energy. The right axis is the rate of monomer conversion, *dM/dt*.

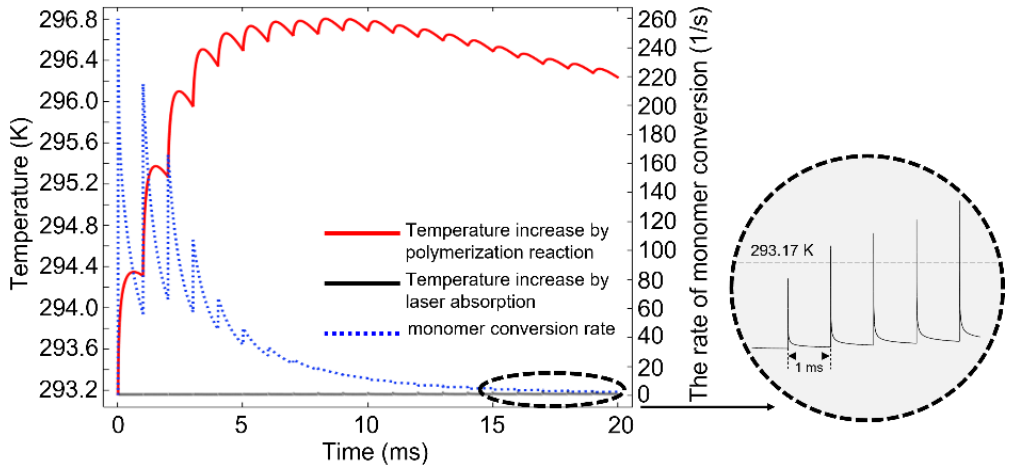

Figure 25. Temperature increase versus time caused by exothermicity of polymerization (solid red curve) and laser absorption (solid black curve). The rate of monomer conversion versus time is plotted as the dotted blue curve (f = 1 kHz, E_p = 6 μJ).

The monomer conversion rate jumps with each laser pulse, and then rapidly drops. The conversion rate drops between laser pulses due to the combined effects of oxygen quenching, *R-R* recombination, and slowing of the propagation rate per Equation 12. Each of these effects

contributes to varying amounts over the total exposure time. For example, oxygen quenching is only significant for the first pulse, but insignificant thereafter because oxygen is locally depleted. With each subsequent pulse, more radicals are formed, so the conversation rate rises again. But the rise is less than for earlier pulses because the concentration of photonitiator steadily decreases with each pulse, and it is not replenished by diffusion. After about 10 pulses, the photoinitiator is consumed, so the rate of monomer conversion simply decreases with time.

Throughout irradiation, the temperature change is modest, and the overwhelming majority of heating results from the exothermicity of polymerization. Heating due to absorption of laser light increases the temperature by no more than ~0.03 K (see inset), because two-photon absorption is weak, and the material has negligible one-photon absorption. Because monomer conversion *c* increases throughout the exposure, heating due to laser absorption actually increases continuously. The temperature increases due to absorption are overwhelmed by heating from polymerization, and even that rises by no more than 4 K, reaching a peak of 296.8 K after approximately 10 pulses. As the polymerization slows, heat within the irradiated volume diffuses to the surroundings, and the temperature drops.

Similar results were reported by Mueller et al. The authors experimentally measured temperature *in situ* within the irradiation volume during TPP and found it rose by no more than approximately 5 K under relevant fabrication conditions ($P \leq 10$ mW, effective exposure time = 20 ms) [39]. When the volume is overexposed, causing damage, much higher temperature increases result (100 K - 300 K) [39]. Micro-explosions (bubble formation due to boiling of monomer) have also been reported elsewhere. The sudden rise in temperature has been attributed to nonlinear process like photoionization and formation of plasma. These effects are not modeled in the present work.

4.2. Fabrication Time and Energy Demand under Different Irradiation Conditions

A key research thrust in TPP is to substantially decrease fabrication time without compromising TPP's sub-micrometer resolution. Figure 26(a) plots the behavior of fabrication time needed to polymerize a single voxel by reaching its photopolymerization threshold (60%) under laser irradiation conditions of different single pulse energy levels (up to 15 μJ) and repetition rates (up to 100 kHz). The plot exhibits a saddle shape. A collection of laser irradiation conditions that yield the shortest fabrication time can be found in the valley region of this plot. The valley region is axisymmetric about the origin and the (15 μJ, 100 kHz) line. Under conditions of low pulse energy and low repetition rate, fabrication time increases due to termination by oxygen inhibition. The oxygen dissolved in the resin acts as a quencher by attaching to both the primary radicals and propagating radicals. They yield fewer active peroxide radicals, which cannot participate in further polymerization reactions. The number of generated radicals is significantly reduced under irradiation conditions of low laser energy and lower repetition rate. They are immediately scavenged by oxygen and make no contribution to polymerization reaction. As a consequence, oxygen quenching slows down polymerization reaction as the chain reaction will not be able to propagate until the oxygen molecule concentration is greatly reduced [13]. When TPP is performed under irradiation conditions with high single pulse energy and high repetition rate, the vast majority of the generated radicals become wasted, as the quadratic radical-radical recombination terminates the chain propagation, so that fabrication time is lengthened as well.

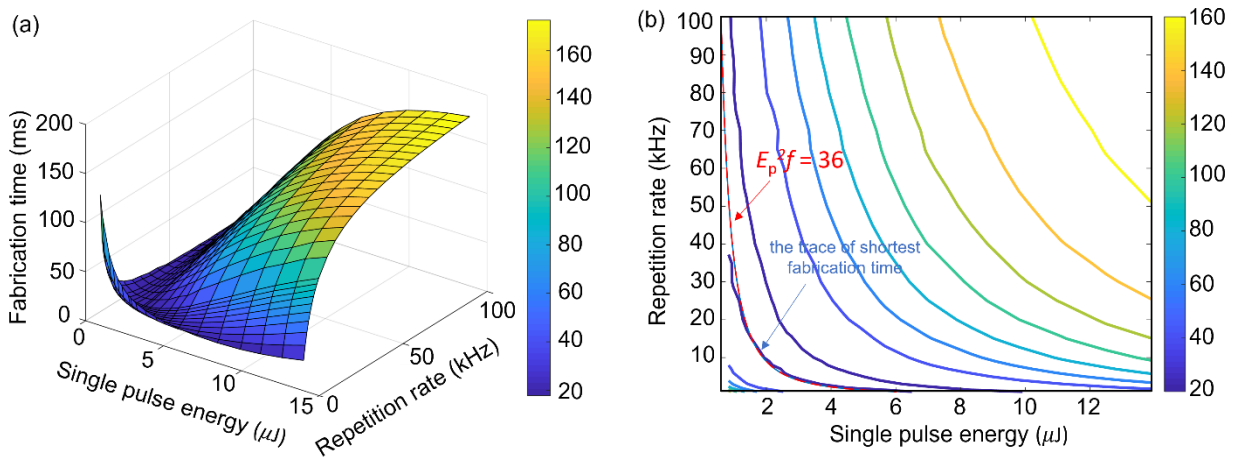

Figure 26. (a) Fabrication time needed to polymerize a single voxel under different laser irradiation conditions. (b) Contours of identical fabrication time obtained under a set of laser irradiation conditions having $E_p^2 f$ = *Constant.*

Figure 26(b) shows that identical fabrication time can be obtained under a set of laser irradiation conditions that satisfy $E_p^2 f$ = Constant, where E_p is pulse energy (μJ), f is repetition rate (kHz). This relation can be interpreted as that equal absorbed total energy ($E_p^2 f$) contributes to similar fabrication time. The power of two in $E_p^2 f$ comes from the nonlinearity of two-photon absorption. Radicals are generated by the decomposition of the photoinitiators that undergo laser irradiation at the focal volume. The decomposition rate of photoinitiators depends on the square of applied photon flux φ, which is proportional to the applied laser intensity I and single pulse energy given a constant pulse duration. For instance, the trace of shortest fabrication time (19 ms) corresponds to the relationship of $E_p^2 f$ = 36, which is plotted as the red dotted curve in Figure 26(b), so all the combinations of single pulse energy and repetition rate on the dark blue trace yield similar fabrication time. For instance, a voxel can be polymerized in 19 ms by an irradiation of 0.6 μJ single pulse energy at 100 kHz repetition rate (1900 total pulses), and the same fabrication time can also be achieved by an irradiation of 6 μJ single pulse energy at 1 kHz repetition rate (19 total pulses).

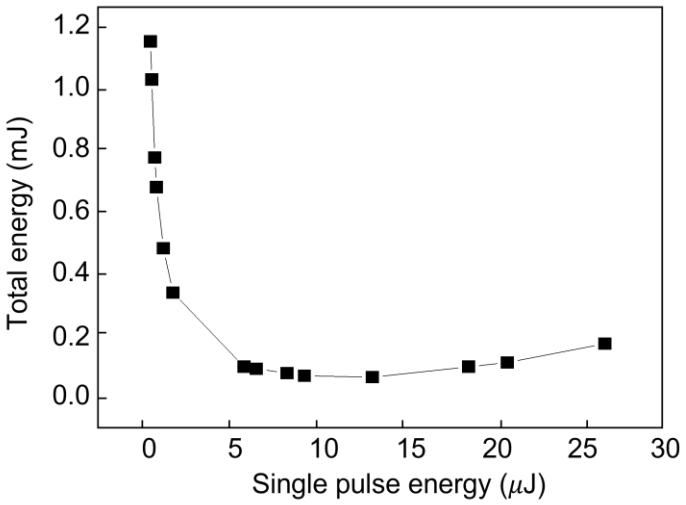

Figure 27. The total energy under a set of laser irradiation conditions (E^2f = 36*)* that yield shortest fabrication time.

In addition to decreasing fabrication time, it is also important to explore the most energy-efficient way of delivering the laser energy to achieve a single polymerized voxel. It is found that the energy demands on each iso-fabrication time contour ($E_p^2 f = Constant$) are different. Figure 27 depicts the energy demand under a set of laser irradiation conditions ($E_p^2 f$ = 36) that yields the shortest fabrication time. It is observed that when single pulse energy is lower than 10 μJ, energy demand decreases as single pulse energy increases; however, when single pulse energy increases beyond 10 μJ, the opposite trend is displayed because of the strong termination caused by quadratic radical-radical (*R*-*R*) recombination. While the exact values vary in different TPP systems, Figure 27 shows that in a process where the total laser energy is the constraint, there exists an optimal combination of pulse energy and repetition rate, which yields the lowest total laser energy to fabricate a single voxel.

4.3. Influence of Quadratic Radical-Radical Recombination

To study the effect of radical-radical recombination, simulations were run with and without the term of $2k_tR^2$ in Equation (11) (all other parameters are identical) and the concentration of radicals was plotted over 25 pulses. Under both conditions, the contribution of

each laser pulse to creating additional radicals can be observed, but the step-like increase becomes less and less till reaching equilibrium as photoinitiator concentration decreases. The red dotted curve (W/O *R*-*R* recombination) continues to rise until it approaches the same concentration as that of the photoinitiator when reaction starts. The blue curve (W *R*-*R* recombination) has a sharp increase when one pulse arrives, and then decays rapidly and increases again when the next pulse is delivered. This comparison of trends indicates that a large number of the generated radicals can become wasted due to *R*-*R* recombination. The termination becomes more severe when a high radical concentration is present as indicated by the term of $2k_tR^2$ in Equation (11).

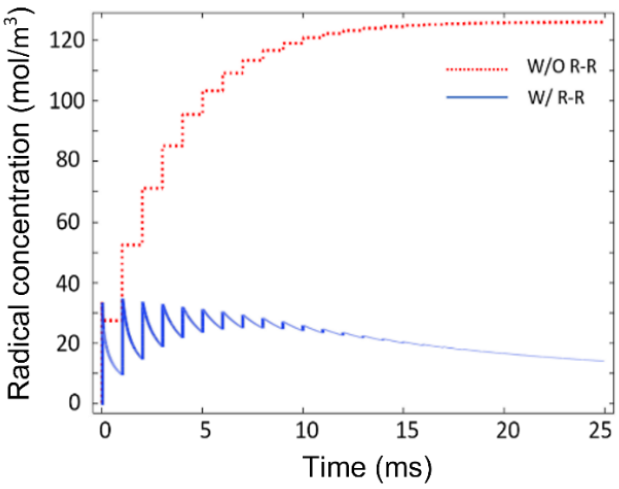

Figure 28. The radical concentration with and without termination by radical-radical (R-R) recombination (6 μJ pulses and f = 1 kHz).

Figure 29 shows radical waste percentage under different laser irradiation conditions. The repetition rate ranges from 100 Hz to 100 kHz, and the single pulse energy spans from 0.5 μJ to 30 μJ. The waste percentage is calculated as the summation of all terminated radicals divided by the summation of all generated radicals during the entire fabrication time (the time it takes for a single voxel to reach its photopolymerization threshold). Figure 29(a) shows the radical waste

percentage at the repetition rate of 100 Hz. In the regime of single pulse energy below 10 μJ, radical loss is more severe at lower pulse energy due to scavenging of free radicals by oxygen quenching termination reactions. Whereas in the regime of stronger laser pulse (10 μJ - 30 μJ), an increase of single pulse energy gives a higher percentage of radical waste (up to 98.87%), caused by the reaction of quadratic radical-radical recombination. Figure 29(d) depicts the radical waste percentage at the repetition rate of 100 kHz. A large number of pulses are delivered during the fabrication time and generate a decent amount of radicals. However, it turns out that approximately 98% radicals are terminated when the single pulse is greater than 1 μJ due to the quadratic radical-radical recombination. Figures 29(b) and 29(c) demonstrate radical waste percentage at the repletion rate of 1 kHz and 10 kHz, respectively. Overall, the majority of radicals (> 55%) are terminated by the reaction of quadratic *R*-*R* recombination, and an increase of single pulse energy gives a higher percentage of radical waste (up to 98.87%).

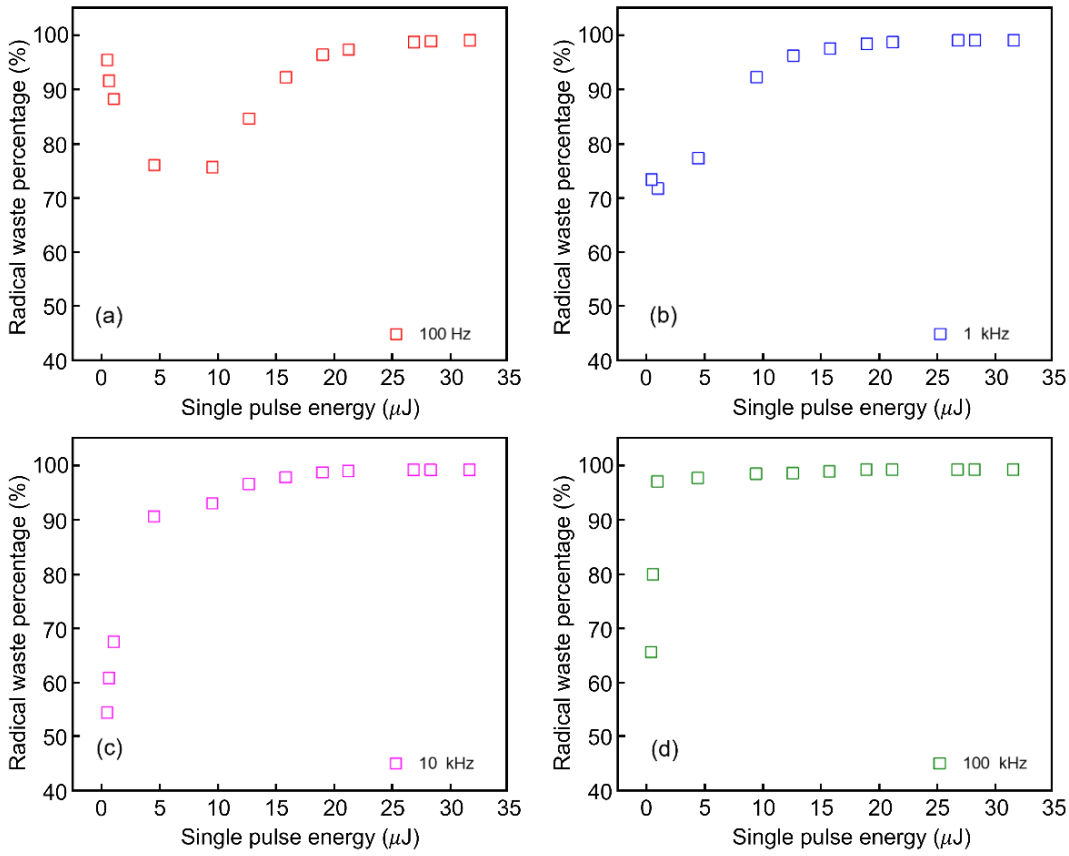

Figure 29. Radical waste percentage under different laser irradiation conditions.

Figure 30(a) shows how laser intensity influences monomer conversion for different numbers of pulses applied (1, 5, 10, 20, and 50 pulses). This set of simulations is conducted using a fixed repetition rate of 1 kHz, so the fabrication time to execute the pulse numbers are 1 ms, 5 ms, 10 ms, 20 ms, and 50 ms, respectively. Overall, for a given laser intensity, monomer conversion increases as more pulses are delivered. The same monomer conversion can be achieved by a larger number of low intensity pulses and also by fewer high intensity pulses. Figure 30(a) also indicates that too few pulses (<< 20) cannot polymerize a voxel above the photopolymerization threshold (60%). For a fixed fabrication time, monomer conversion first rises as laser intensity increases, and then it decreases (or plateaus in the case of 1 pulse) as laser intensity continues to increase. This transition is believed to be the result of radical termination

by the strong quadratic *R-R* recombination induced by high intensity laser pulses. A similar phenomenon is also observed in Figure 30(b), where the maximum monomer conversion doesn't occur at the peak laser intensity. This is because at high laser intensity, strong quadratic *R-R* recombination can take place that decreases the active radicals to react with monomer molecules. In this case, laser energy is utilized inefficiently when delivered as fewer high-intensity pulses.

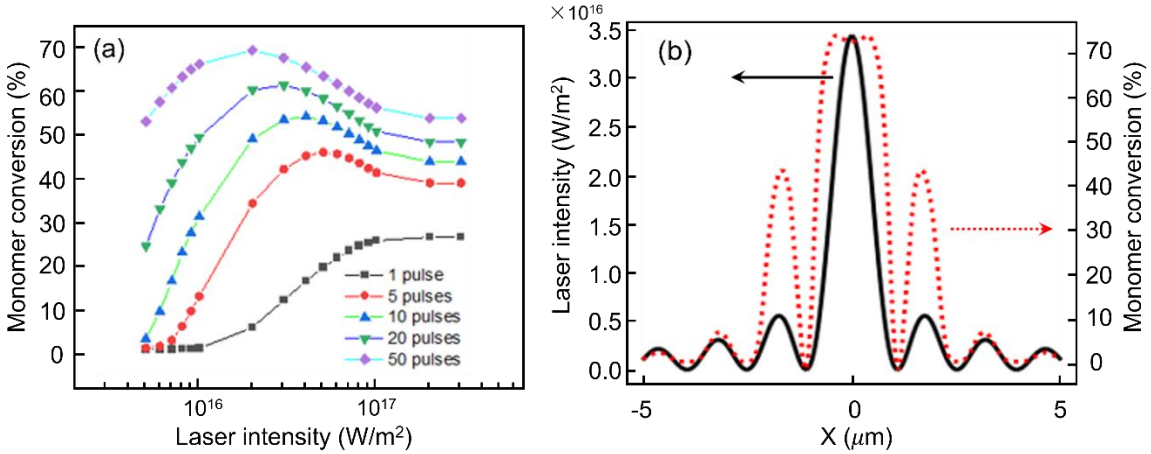

Figure 30. (a) The influence of laser intensity on monomer conversion (number of pulses = 1, 5, 10, 20, and 50). (b) Monomer conversion along the radical direction.

4.4. Conclusions of Two-Photon Polymerization Additive Manufacturing

This paper presents a mathematical framework to model TPP activated with Bessel beams under a wide range of pulse-repetition rates, energies, and spatio-temporal regimes. The investigated laser operational regime is different from a conventional megahertz repetition rate laser system. A femtosecond laser is operated with low repetition rate (0.1 kHz - 100 kHz) and high peak intensity (10^{15} W m^{-2} - 10^{17} W m^{-2}). Results show that the number of pulses needed to polymerize a voxel in this regime is significantly lower than the ten thousand to ten million cumulative laser pulses needed by a megahertz repetition rate laser. The required fabrication time is also shortened while maintaining the superb sub-wavelength feature resolution of two-photon polymerization. There exists a shortest fabrication time for a single voxel to be polymerized above a monomer conversion threshold under a set of irradiation conditions (single pulse energy and repetition rate combinations). In low single pulse energy regime (< 10 μJ), it is more energy-efficient to use fewer and higher-energy pulses within the same fabrication time. However, this trend reverses when the termination by *R*-*R* recombination becomes more severe in the regime of high single pulse energy (10 μJ - 30 μJ), where over 90% of the generated radicals are wasted due to radical-radical recombination. Also, in the investigated regime, the local temperature increase during the entire fabrication time is negligibly small and is mainly attributed to the exothermic polymerization reaction.

Chapter 5 - Future Research

5.1. Modelling for Scanning Beams

The presented mathematical model of two-photon photopolymerization is for stationary laser exposures. It can be modified for modeling a tightly focused scanning laser beam to solidify photopolymer resin in a layer-by-layer manner. For the 3D microdevices fabricated by two-photon polymerization, resolution and writing speed are two critical factors. The former dominates the smallest feature size, and the latter limits the process yield rate. This built model can be used as a practical tool to investigate the fundamental mechanism of the interplay of resolution and writing speed.

5.2. Programming Mechanical Properties by Laser Parameter Selection

It has been reported that the mechanical properties of acrylate-based resins are related to the degree of conversion, which itself correlates with the exposure dose of light during fabrication [40].

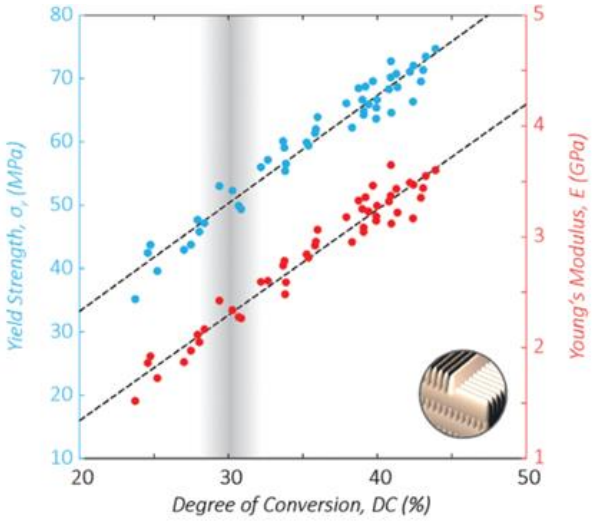

Figure 31. The dependence of E and σ_y on DC. Copyright Advanced Materials Technologies 4, no. 9 (2019): 1900146.

The developed model can predict the degree of conversion during TPP fabrication under various irradiation conditions, therefore it can be potentially used to predict the processing-structure-properties relation and optimize the properties of TPP fabricated structures, which lays the foundation for a universal quantitative predictability of the mechanical properties of TPP-derived materials.

5.3. Engineering Beam Wavefront

In addition to the zeroth order Bessel beam, the built model may be expected to transfer to other beam shapes, such as high order Bessel beams, twisting laser beams, ring laser beams, and so on. The investigation of different beam shapes will provide meaningful knowledge for ongoing effort to overcome major technological challenges of TPP, including increasing the resolution, decreasing fabrication time, and improving mechanical properties.

PART II – Ultrasonic-Assisted Manufacturing for Biomass-based Products

Low energy and volumetric density of biomass has been a major challenge hindering its large-scale utilization as a bioenergy resource. Torrefaction is a thermochemical pretreatment process that can significantly enhance the properties of biomass as a fuel by increasing the heating value and thermal stability of biomass materials. Densification of biomass by pelleting can greatly increase the volumetric density of biomass to improve its handling efficiency. Currently, torrefaction and pelleting are processed separately. So far there has been little success dovetailing torrefaction and pelleting that only requires a single material loading to produce torrefied pellets. Synchronized ultrasonic torrefaction and pelleting has been developed to address this challenge. Synchronized ultrasonic torrefaction and pelleting can produce pellets of high energy and volumetric density in a single step, which tremendously reduces the time and energy consumption compared to that required by the prevailing multi-step method. This novel fuel upgrading process can increase biomass temperature to 473-573 K within tens of seconds to create torrefaction. Studying the temperature distribution is crucial to understand the fuel upgrading mechanism since pellet energy density, thermal stability, volumetric density, and durability are all highly related to temperature. A rheological model was established to instantiate biomass behaviors when undergoing various ultrasonic vibration conditions. Process parameters including ultrasonic amplitude, ultrasonic frequency, and pelleting time were studied to show their effects on temperature at different locations in a pellet. Results indicated that the volumetric heat generation rate was greatly affected by both ultrasonic amplitude and frequency. This model can help to understand the fuel upgrading mechanism in synchronized ultrasonic

torrefaction and pelleting and also to give guidelines for process optimization to produce high quality fuel pellets.

Chapter 1 - Literature Review of Synchronized Ultrasonic Torrefaction and Pelleting

1.1. The Significance of Biomass Energy

The excessive use of fossil fuels, accumulation of greenhouse gases, and rapid growth of global population have increased worldwide interests in a variety of renewable energy such as biomass, solar, wind, geothermal, and hydroelectric energy. Among all of the renewable energy, biomass has been considered as a promising resource because of its wide distribution and vast abundance on the earth [41]. Moreover, utilizing biomass as an energy resource has advantages of decreasing pollutant generation and lowering net carbon emissions. All carbon contained in biomass is gained from carbon dioxide in the atmosphere through photosynthesis; in other words, the carbon dioxide produced when biomass is consumed as a fuel is recycled when new crops and plants grow [42]. Therefore, biomass has been regarded as a carbon-neutral fuel resource. There is an urgent need to efficiently derive bioenergy from biomass to reduce greenhouse gas emissions, lower the dependency on limited fossil fuels, and improve national energy security. The following sections review the composition, structure, and properties of lignocellulosic biomass, and states the conventional biomass preprocessing and pretreatment methods.

1.2. Composition and Structure of Lignocellulosic Biomass

The major chemical compositions of lignocellolosic biomass can be characterized by three components: cellulose, hemicelluloses, and lignin, which together form a complex and rigid structure (Figure 32). Cellulose is a linear crystalline biopolymer. Coupling of adjacent cellulose chains by orderly hydrogen bonds and van der Waal’s forces lead to parallel alignment and a crystalline structure. Hydrogen bonds maintain and reinforce the flat linear conformation

of the chain. The top and bottom of the cellulose chains are essentially completely hydrophobic. The sides of the cellulose chains are hydrophilic and capable of bonding hydrogen because all the aliphatic hydrogen atoms are in axial positions, whereas the polar hydroxyl groups are in equatorial positions [43].

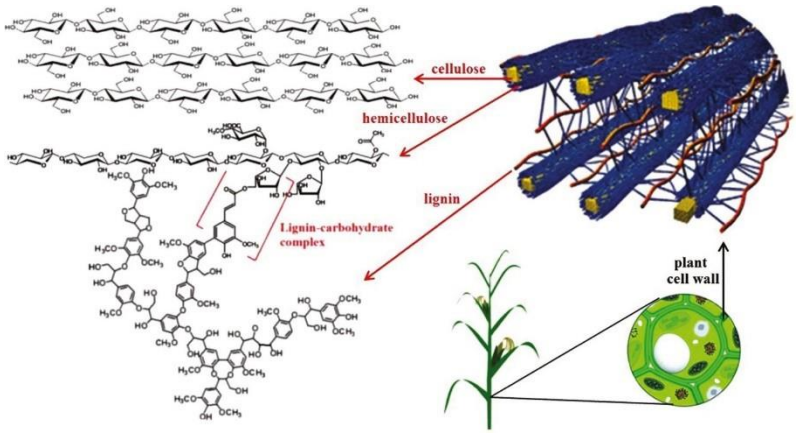

Figure 32. Composition and structure of lignocellulosic biomass. Copyright Applied microbiology and biotechnology 104, no. 12 (2020): 5201-5212.

Hemicellulose is a complex amorphous polymer, situated between lignin and a collection of cellulose fibers underneath. The most abundant building block of hemicellulose is xylan, which plays an important role in maintaining the integrity of the plant cell wall by using its covalent linkage to lignin and its non-covalent interaction with cellulose [43-44].

Lignin is an irregular polymer, which is synthesized via enzyme-initiated free radical polymerization of the alcohol precursors, such as coumaryl alcohol, coniferyl alcohol, and sinapyl alcohol. The dehydrogenation of these alcohol monomers form both C-C bond and C-O bonds, leading to a heterogeneous three-dimensional structure. Additional components of lignin such as hydroxycinnamic acids and flavonoids further complicate the structure and decorate the aromatic heteropolymer with additional linkages and chemical functionality [43-44].

1.3. Viscoelasticity of Lignocellulosic Biomass

Viscoelasticity is the property of materials that exhibit both viscous and elastic characteristics when undergoing deformation [45-49]. For instance, synthetic polymers, wood, and biological soft tissue display significant viscoelastic effects. Generally, viscoelastic materials are those for which the relationship between stress and strain depends on time, and they possess the following three important properties: stress relaxation, creep, and hysteresis (a stress-strain phase lag).

Biomass consists mainly of three compositional polymers: cellulose, hemicellulose, and lignin. These are associated together in a hetero-matrix, which can be considered a viscoelastic material, exhibiting both elastic and viscous characteristics when undergoing deformation. The former can be regarded as elastic energy stored in a spring, the latter is associated with viscous energy dissipation as in a dashpot contenting a Newtonian liquid.

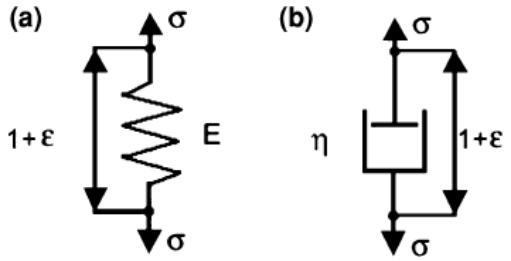

Figure 33. Basic elements of (a) spring and (b) dashpot

The mechanical behavior of viscoelastic material has been found to be complex when stress is applied, exhibiting time-dependent stress-strain characteristics. There are a number of rheological models, Maxwell model and Kelvin-Voigt model are the most usual idealizations of the viscoelastic characteristics of a real material. This work presents a generalized Maxwell model to exemplify the biomass behaviors under various ultrasonic vibration conditions.

1.4. Conventional Biomass Preprocessing and Pretreatment Methods

The utilization of biomass to produce bioenergy has been growing rapidly. For instance, biomass can be utilized as gaseous or liquid fuels through a variety of conversion methods via both thermochemical and biochemical platforms such as gasification, pyrolysis, anaerobic digestion, and fermentation. Biomass can also be converted into solid fuels such as fuel pellets for power generation at a co-fired power plant or for syngas generation by gasification. However, most of these applications are still limited to pilot scales due to the characteristics of biomass feedstock, including its low energy and volumetric density and high hydrophilicity. These challenges contribute to the low energy conversion efficiency of biomass and result in a high logistic cost of transporting and storing biomass feedstock [50,51]. Over the last decade, there have been a number of biomass preprocessing methods developed to address these challenges. Torrefaction and pelleting are the two most recognized methods to preprocess biomass for solid fuel production [52,53].

1.4.1. The Torrefaction Process

Biomass torrefaction has been recognized as a technically feasible method of converting raw biomass into a solid fuel that is suitable for commercial and residential combustion applications. Torrefaction involves the heating of biomass in the absence of oxygen to a temperature of typically 473K to 573K (200 - 300°C), which results in thermal degradation of its structure [54].

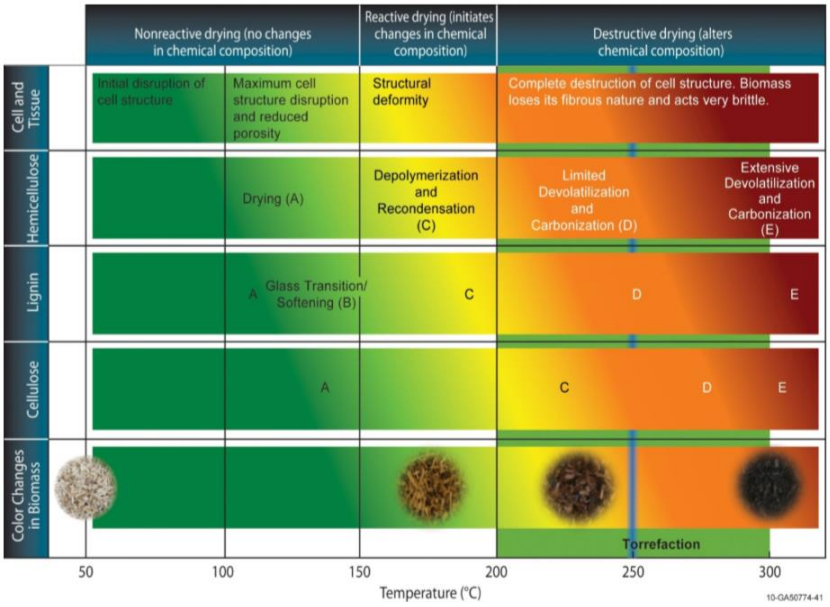

Figure 34. Structural, chemical, and color changes in biomass at different drying temperatures. Copyright Renewable and sustainable energy reviews 57 (2016): 1126-1140.

During the initial heating of lignocellulosic materials, most of the moisture is removed and lignin becomes soft at temperatures between 433K and 453K (160 - 180°C). At temperatures of 453K - 543K (180 - 270°C), lignin continues to degrade and begins to exhibit thermosetting properties, which make lignin permanently rigid and likely to bond together with other components of biomass. Also at the temperature range of 453K - 543K (180–270°C), hemicellulose significantly decomposes caused by chemical reactions such as devolatilization and carbonization, resulting in a destructive lignocellulosic structure. Cellulose also undergoes depolymerization and devoltilization in the range of temperatures at which torrefaction is normally carried out, but within a narrow temperature band of 543K – 573K (270–300°C). At temperatures above 553 K (280°C), the chemical reactions are mostly exothermic, leading to an increase in the production of condensable and non-condensable gases such as CO, hydrocarbons (phenols and cresols), and other heavier products. For the torrefaction process, temperatures over

573K (300°C) are not recommended as these may lead to extensive devolatilization of the biomass [55].

1.4.2. The Pelleting Process

There have been attempts to overcome the poor handling properties of biomass (low bulk density and inhomogeneous structure) by employing densification technologies, such as bailing, briquetting, extrusion, and pelleting [56]. The present review is limited to the technique of pelleting. The pelleting process consist of multiple steps, which include raw material pre-treatment, pelletization, and post-treatment. Pre-treatment steps generally consist of size reduction, drying, and conditioning. After pelletization, the pellets are transferred into a pellet cooler and screened to remove small particles.

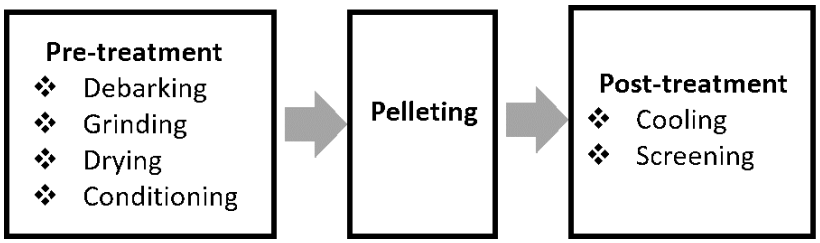

Figure 35. A typical overview of the biomass densification process

Pellets are produced in a mill that generally consist of a die with cylindrical press channels and rollers that force the biomass to flow into and through the channels. Due to the friction between the steel surface and the biomass in the press channel, a high back pressure is built-up and heat is generated. A die with press channels and rollers are the basic parts of a pellet mill. The die can either be in the shape of a ring or a flat plate, as shown in Figure 36 [56]. Either the die or the rollers can be rotating, and due to that movement, the biomass particles are squeezed into the openings of the press channel and a layered structure of the pellet is produced.

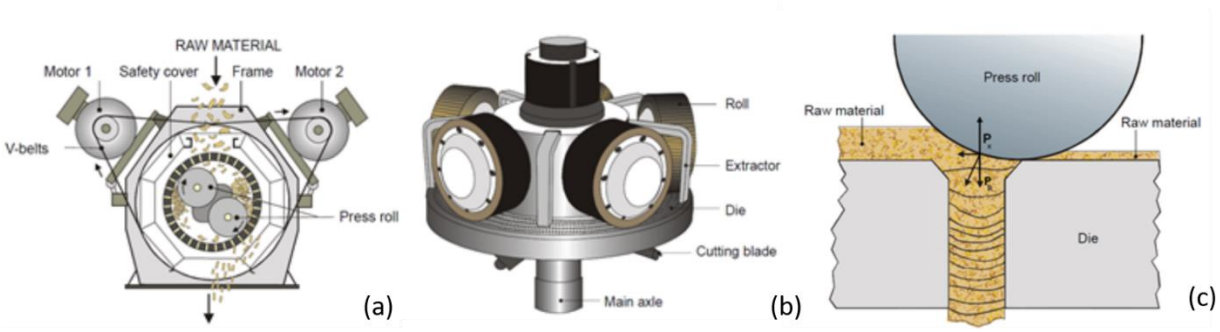

Figure 36. Pellet mill design with (a) ring die and (b) flat die, (c) Assembly of a pellet in the press channel of a pellet mill. Copyright BioResources, 7(3), pp.4451-4490.

1.5. Synchronized Ultrasonic Torrefaction and Pelleting

When torrefaction is combined with pelleting, a biomass preprocessing method of compacting biomass into pellets of high density, the volumetric density of torrefied biomass can be significantly increased [57-59]. Currently, torrefaction and pelleting are two separate processes. In order to make torrefied biomass pellets, torrefaction is usually conducted first, which requires moderate to high temperatures and a long reaction time. Torrefied biomass is then agglomerated into pellets in a separate pelleting process [60]. Pelleting torrefied biomass is more difficult under the same operating conditions as those used for pelleting untreated biomass. Before pelleting, the addition of binding agents to condition the torrefied biomass also increases the time and energy consumption in a torrefied pellet production facility [61].

To address the aforementioned challenges, synchronized ultrasonic torrefaction and pelleting is developed. This method employs ultrasound energy to realize simultaneous torrefaction and pelleting with a single material loading. In the preliminary experiments, synchronized ultrasonic torrefaction and pelleting can reduce the time and energy consumptions without compromising the pellet quality provided by the prevailing solution. It produces durable torrefied pellets with high volumetric density, high energy density, and good hydrophobicity [62].

Chapter 2 - Experimental Setup for Synchronized Ultrasonic Torrefaction and Pelleting

2.1. Biomass Preparation

The biomass used in this study was wheat straw, harvested and collected in northwestern Kansas. Afterwards, the wheat straw was transported to and stored in the lab, where it was size reduced into small particles. A knife mill (Model SM 2000, Retsch, Inc., Haan, Germany) installed with a 2 mm sieve was used to control the biomass particle size. The majority of the 2 mm wheat straw particles were stored in sealed plastic bags at room temperature.

2.2. Experimental Setup for Ultrasonic Vibration Amplitude Measurement

Ultrasonic horn is responsible for amplifying the ultrasonic vibration generated by piezoelectric discs and transferring ultrasonic vibration from the transducer onto biomass. A non-contact capacitive sensor (Elite Series CPL490, Lion Precision, St. Paul, MN, USA) was employed to measure the vibration amplitude at the output end of the ultrasonic horn. The capacitive sensor was fixed vertically up as shown in Figure 37, and the tip of the sensor was positioned with a gap of approximate 25 um away from the output end of the ultrasonic horn before the measurement. Due to its non-contact nature, the capacitive sensor does not affect the motion of the output end of the horn or dampen its vibration amplitude. When the electrical input was applied to the ultrasonic system, the gap was narrowed or expanded as the ultrasonic horn vibrated perpendicularly. The changes in the gap were captured by the sensor, which were then converted into DC voltages between –10 and +10 V. The DC voltage has a proportional dependence on the change of the gap between the capacitive sensor and the ultrasonic horn. The

actual vibration amplitude was determined by using the displacement sensitivity (0.4 V/mm). More details describing this measurement approach can be found in [63].

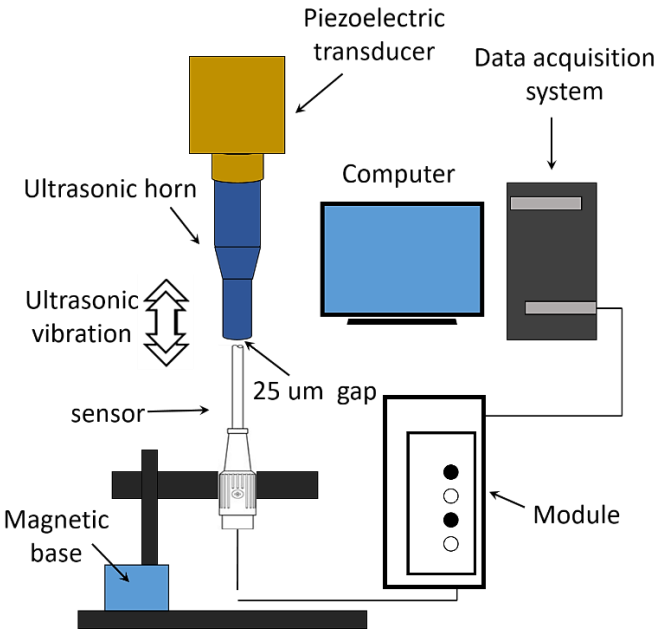

Figure 37. Schematic of the ultrasonic vibration amplitude measurement system

2.3. Experimental Setup for Synchronized Ultrasonic Torrefaction and Pelleting

An experimental platform, where all the synchronized ultrasonic torrefaction and pelleting experiments were performed, was customized from an ultrasonic machine as shown in Figure 38, the experimental platform has three major systems including an ultrasonic vibration generation system, a pneumatic loading system, and a temperature measurement system.

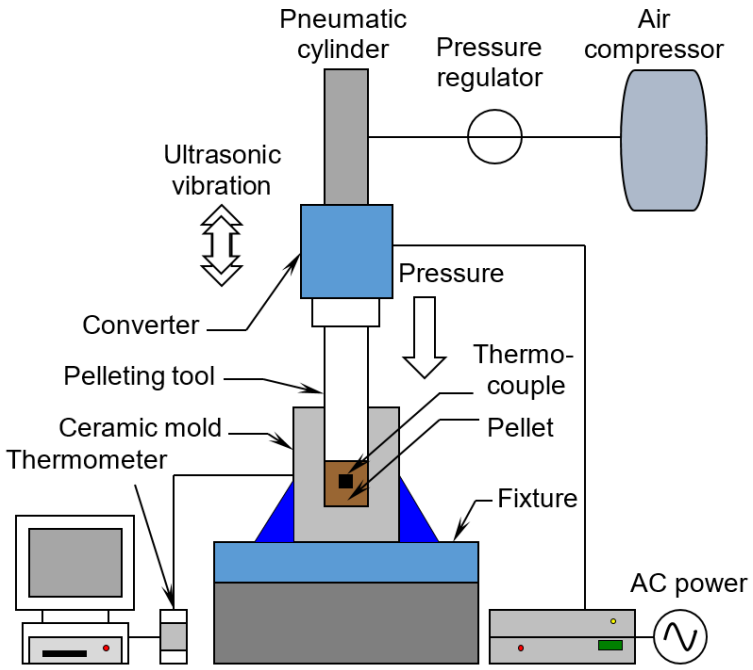

Figure 38. Schematic illustration of the experimental setup for synchronized ultrasonic torrefaction and pelleting

The ultrasonic vibration generation system is comprised of an ultrasonic power supply, a piezoelectric converter, and a titanium pelleting tool with a flat-ended cylindrical tip. The ultrasonic power supply contributes to providing 20 kHz high frequency electric power. The transformation of electric power to mechanical vibration is realized by the piezoelectric converter, a crystal that produces mechanical stress in response to an applied electrical field. The ultrasonic vibration is then amplified and transmitted to the pelleting tool, which results in the perpendicular vibration of the pelleting tool at the same frequency as the electrical power. The vibration amplitude is controllable by regulating the ultrasonic power supply. The relationship between ultrasonic power, ultrasonic amplitude, and ultrasonic power percentage is listed in Table 2.

Table 2. Relationships between ultrasonic power, ultrasonic amplitude, and ultrasonic power percentage

Ultrasonic power (W)	Ultrasonic amplitude (um)	Ultrasonic power percentage (%)

100	18	20
150	20	30
200	25	40
250	28	50

The pneumatic loading system, utilized to provide pelleting pressure, consists of an air compressor, a pressure regulator, and a pneumatic cylinder. The air pressure in the pneumatic cylinder is controlled by the pressure regulator. Before making a pellet, biomass particles are loaded into a mold made of glass ceramic (Model Macor, Corning Incorporated, NY, USA) that consists of two parts: the upper part forms a cylindrical cavity and the bottom part is a square plate serving as a base.

The temperature measurement system includes a thermocouple (Model SC-GG-K-30-36, OMEGA Engineering, Inc., Stamford, CT, USA), embedded in the middle of the pellet to measure the temperature at the pellet center, a thermometer (Model HH147U, OMEGA Engineering, Inc., Stamford, CT, USA), and a computer with a data acquisition software package.

Chapter 3 - Multiphysics Modeling of Ultrasound-Assisted Biomass Torrefaction

In this chapter, a simplified temperature model is presented in Section 3.1, assuming all the ultrasonic energy was absorbed by biomass and converted into heat. It serves as a bottom line to compare with the viscoelastic heating temperature model, which is presented in Section 3.2 and driven by the hypothesis that biomass viscoelastic heating induced by ultrasonic vibration causes synchronized torrefaction and pelletizing to occur.

3.1. A Simplified Temperature Model

3.1.1. Model Description

When an ultrasound wave propagates through a volume of biomass medium, the majority of the energy in the acoustic field is absorbed locally by the biomass, resulting in the generation of heat. This torrefaction effect results in a temperature increase of the biomass, converting biomass into a coal-like intermediate with upgraded fuel properties over the original biomass. A simplified temperature model was established, assuming all the ultrasonic energy was absorbed by biomass and converted into heat without considering the heat generation mechanism. It served as a bottom line to compare with the viscoelastic heating temperature model.

3.1.1.1. Model Assumptions

The model consists of four components: piezoelectricity model for transducer, linear elastic material model for ultrasonic horn, pressure acoustics model for biomass, and heat transfer model for temperature increase. Several major assumptions are involved in the development of the model:

(1) The transducer and the ultrasonic horn vibrate in longitudinal mode only.

(2) The transducer and the ultrasonic horn are assumed to be isotropic linear elastic materials.

(3) The effects of elements such as bolts and electrodes of the ultrasonic system are neglected.

(4) Piezoelectric ceramics respond linearly to changes in the electric field.

(5) Biomass particles are compressed into solid at the initial stage and fill the mold continuously; hence, biomass in the mold is assumed to be homogeneous.

(6) The initial temperature of the system is ambient temperature.

(7) The heat flux at the boundaries of different materials is continuous.

3.1.1.2. Piezoelectricity Model for Transducer

The piezoelectric transducer consists of four PZT discs, there is a thin metal plate between each two of the discs, which forms the electrode. As the input electrical signal applied to the transducer via the electrodes, PZT discs expand and contract to produce a mechanical vibration. In this section, the piezoelectricity constitutive equations are given by Equations (29) and (30). The behavior of PZT discs is represented in a stress-charge form, which relates stress, strain, electric field, and electric displacement field [64]:

$$T = c^E S - eE \tag{29}$$

$$D = e^t S + \varepsilon^S E \tag{30}$$

Where T is the matrix (6×1) of the stress; D is the matrix (3×1) of the electric displacement; E is the matrix (3×1) of the electric field strength; S is the matrix (6×1) of the strain; C^E, e, and ε^S are material properties corresponding to the matrix (6×6) of material stiffness, the matrix (6×3) of the PZT coupling properties, and the matrix (3×3) of relative permittivity at constant strain, respectively; superscript t denotes a transposed matrix, thus, e^t is

the matrix (3×6) of the converse PZT coupling for stress-charge. Using the Voigt notation and writing out the components gives:

$$\begin{pmatrix} T_{xx} \\ T_{yy} \\ T_{zz} \\ T_{yz} \\ T_{xz} \\ T_{xy} \end{pmatrix} = \begin{pmatrix} c_{11}^E & c_{12}^E & c_{13}^E & c_{14}^E & c_{15}^E & c_{16}^E \\ c_{21}^E & c_{22}^E & c_{23}^E & c_{24}^E & c_{25}^E & c_{26}^E \\ c_{31}^E & c_{32}^E & c_{33}^E & c_{34}^E & c_{35}^E & c_{36}^E \\ c_{41}^E & c_{42}^E & c_{43}^E & c_{44}^E & c_{45}^E & c_{46}^E \\ c_{51}^E & c_{52}^E & c_{53}^E & c_{54}^E & c_{55}^E & c_{56}^E \\ c_{61}^E & c_{62}^E & c_{63}^E & c_{64}^E & c_{65}^E & c_{66}^E \end{pmatrix} \begin{pmatrix} S_{xx} \\ S_{yy} \\ S_{zz} \\ S_{yz} \\ S_{xz} \\ S_{xy} \end{pmatrix} + \begin{pmatrix} e_{11} & e_{21} & e_{31} \\ e_{12} & e_{22} & e_{32} \\ e_{13} & e_{23} & e_{33} \\ e_{14} & e_{24} & e_{34} \\ e_{15} & e_{25} & e_{35} \\ e_{16} & e_{26} & e_{36} \end{pmatrix} \begin{pmatrix} E_x \\ E_y \\ E_z \end{pmatrix} \tag{31}$$

$$\begin{pmatrix} D_x \\ D_y \\ D_z \end{pmatrix} = \begin{pmatrix} e_{11} & e_{12} & e_{13} & e_{14} & e_{15} & e_{16} \\ e_{21} & e_{22} & e_{23} & e_{24} & e_{25} & e_{26} \\ e_{31} & e_{32} & e_{33} & e_{34} & e_{35} & e_{36} \end{pmatrix} \begin{pmatrix} S_{xx} \\ S_{yy} \\ S_{zz} \\ S_{yz} \\ S_{xz} \\ S_{xy} \end{pmatrix} + \begin{pmatrix} \varepsilon_{11}^S & \varepsilon_{12}^S & \varepsilon_{13}^S \\ \varepsilon_{21}^S & \varepsilon_{22}^S & \varepsilon_{23}^S \\ \varepsilon_{31}^S & \varepsilon_{32}^S & \varepsilon_{33}^S \end{pmatrix} \begin{pmatrix} E_x \\ E_y \\ E_z \end{pmatrix} \tag{32}$$

The constitutive equations can also be written in an alternate strain-charge form [64]:

$$S = s^E T + dE \tag{33}$$

$$D = d^t T + \varepsilon^T E \tag{34}$$

Where S^E, d, *and* ε^T are material properties corresponding to the matrix (6×6) of material compliance coefficients, the matrix (6×3) of the PZT coupling for strain-charge, and the matrix (3×3) of relative permittivity at constant stress, respectively. The relations among the coefficients in two different forms are expressed in Equations (35)-(37) [64]:

$$s^E = \left(c^E\right)^{-1} \tag{35}$$

$$\varepsilon^T = \varepsilon^S + d^t \left(s^E\right)^{-1} d \tag{36}$$

$$d = \left(s^E\right) e \tag{37}$$

It is noted that this study employed the piezoelectricity constitutive equations in stress-charge form.

3.1.1.3. Linear Elastic Material Model for Ultrasonic Horn

The transducer and the ultrasonic horn are assumed to be isotropic linear elastic materials. So, the general equation that describes the longitudinal wave propagation along a rigid ultrasonic horn is governed by the Newton's Second Law [65]:

$$\rho \frac{\partial^2 u}{\partial t^2} = \left(\frac{\partial}{\partial x} + \frac{\partial}{\partial y} + \frac{\partial}{\partial z} \right) \sigma + F_V e^{i\phi} \tag{38}$$

where ρ is the mass density of the ultrasonic horn; u denotes the vector of particle displacement in the longitudinal direction; σ is the Cauchy stress tensor; F_V is the body force per unit volume, and $e^{i\varphi}$ represents the AC power supply.

3.1.1.4. Pressure Acoustics Model for Biomass

The pressure acoustics model is used to simulate the acoustic field in the biomass to obtain the acoustic intensity distribution. The acoustic wave equation is given as follows [65, 66]:

$$\left(\frac{\partial^2}{\partial x^2} + \frac{\partial^2}{\partial y^2} + \frac{\partial^2}{\partial z^2} \right) p - \frac{1}{c_b^2} \frac{\partial^2 p}{\partial t^2} = 0 \tag{39}$$

Where p is the acoustic pressure, and c_b is the speed of sound in the biomass. Acoustic pressure is defined as the local pressure deviation from the ambient atmosphere pressure caused by a sound wave propagating through a medium. The acoustic intensity (I) is determined together with acoustic pressure (p) and acoustic particle velocity (v) in a medium and is given in Equation (40) [66], where I is the acoustic intensity and v is the particle velocity.

$$I = pv \tag{40}$$

3.1.1.5. Heat Transfer Model for Biomass Temperature

Equation (41) gives the heat source Q that quantifies the thermal effects associated with the absorption of the ultrasonic wave, where α is the acoustic absorption coefficient [67]:

$$Q = 2\alpha I = 2\alpha \left| \mathrm{Re}\left(\frac{1}{2} pv \right) \right| \tag{41}$$

A spatial-temporal temperature distribution inside the biomass can be solved numerically by the following governing equation:

$$\rho_b C \frac{\partial T}{\partial t} = k\left(\frac{\partial^2}{\partial x^2} + \frac{\partial^2}{\partial y^2} + \frac{\partial^2}{\partial z^2} \right) T + 2\alpha \left| \mathrm{Re}\left(\frac{1}{2} pv \right) \right| \tag{42}$$

where ρ_b is the biomass density; C is the specific heat capacity of biomass; and k is the heat conductivity of the biomass. The material properties of the piezoelectric discs, ultrasonic horn and biomass are listed in Table 3.

Table 3. Material properties of transducer, ultrasonic horn, and biomass

Para.	Description	Value	Ref.
ρ_b	Biomass density	1000 kg/m^3	
c_b	Sound speed in biomass	3848 m/s	
ρ	Titanium density	7850 kg/m^3	[66]
k	Heat conductivity of the biomass	0.34 $W/m{\cdot}K$	[68, 69]
C	Specific heat capacity of biomass	1243 $J/kg{\cdot}K$	[68, 69]
α	acoustic absorption coefficient	3.13 m^{-1}	[68, 69]
E_y	Titanium Young's modulus	205 GPa	
v	Poisson's ratio	0.28	
ρ_t	Transducer density	7500 kg/m^3	[66]
C^E	Matrix (6×6) of elastic coefficients at constant electric field strength	$\begin{bmatrix} 1.27205E11 & 2.34742E10 & 2.29885E10 & & & \\ 2.34742E10 & 8.02122E10 & 2.29885E10 & & & \\ 2.29885E10 & 2.29885E10 & 1.27205E11 & & & \\ & & & 8.46702E10 & & \\ & & & & 8.46702E10 & \\ & & & & & 1.17436E11 \end{bmatrix}$ Pa	[66]
e	Matrix (6×3) of the PZT coupling for stress-charge	$\begin{bmatrix} 0.00000 & 0.00000 & -6.62281 \\ 0.00000 & 0.00000 & -6.62281 \\ 0.00000 & 0.00000 & 23.2403 \\ 0.00000 & 17.0345 & 0.00000 \\ 0.00000 & 17.0345 & 0.00000 \\ 0.00000 & 0.00000 & 0.00000 \end{bmatrix}$ C/m^2	[66]

S^E	Matrix (6×6) of compliance coefficients	$\begin{bmatrix} 1.65E-11 & 4.26E-11 & 4.35E-11 & & & \\ 4.26E-11 & -4.78E-12 & 4.35E-11 & & & \\ 4.35E-11 & 4.35E-11 & 1.65E-11 & & & \\ & & & -8.46E-12 & & \\ & & & & -8.46E-12 & \\ & & & & & 2.07E1-1 \end{bmatrix}$ Pa	[66]
d	Matrix (6×3) of the PZT coupling for strain-charge	$\begin{bmatrix} 0.00000 & 0.000000 & -2.74E-10 \\ 0.00000 & 0.000000 & -2.74E-10 \\ 0.00000 & 0.000000 & 5.93E-10 \\ 0.00000 & 7.41E-10 & 0.00000 \\ 0.00000 & 7.41E-10 & 0.00000 \\ 0.00000 & 0.000000 & 0.00000 \end{bmatrix}$ C / N	[66]
ε^S	Matrix (3×3) of electric permittivity at constant strain	$\begin{bmatrix} 1704.4 & & \\ & 1704.4 & \\ & & 1704.4 \end{bmatrix}$	[66]
ε^T	Matrix (3×3) of electric permittivity at constant stress	$\begin{bmatrix} 3130 & & \\ & 3130 & \\ & & 3400 \end{bmatrix}$	[66]

3.1.2. Model Validation for the Ultrasonic Horn Vibration

Before the developed model is used to predict biomass temperature, its simulation of the ultrasonic horn vibration was first validated to verify if the model can capture the vibration characteristic of the 20 kHz ultrasonic system used in this study. Figure 39 demonstrates the measured vibration amplitude at different electrical power levels (20%, 60%, and 100%) for 0.5 ms. It can be seen that vibration amplitude increased as input electrical power level increased, and the frequency of the vibrations stayed constant at 20 kHz, which coincided with the frequency of the input electrical power. It is also known that in the experimental ultrasonic system, the ultrasonic horn is designed to resonate with 20 kHz input electrical power and produces the highest vibration amplitude at its resonance frequency. This relationship is also confirmed by simulation. Figure 39(b) shows the simulated relationship between peak-to-peak vibration amplitude and the input electrical power frequency. It clearly demonstrates that, at each power level (20%, 60%, or 100%), the highest vibration amplitude occurs when the ultrasonic horn is forced to vibrate at 20 kHz. Besides, as the input electrical power frequency

progressively deviates from 20 kHz, the vibration amplitude decreases until the oscillation nearly disappears.

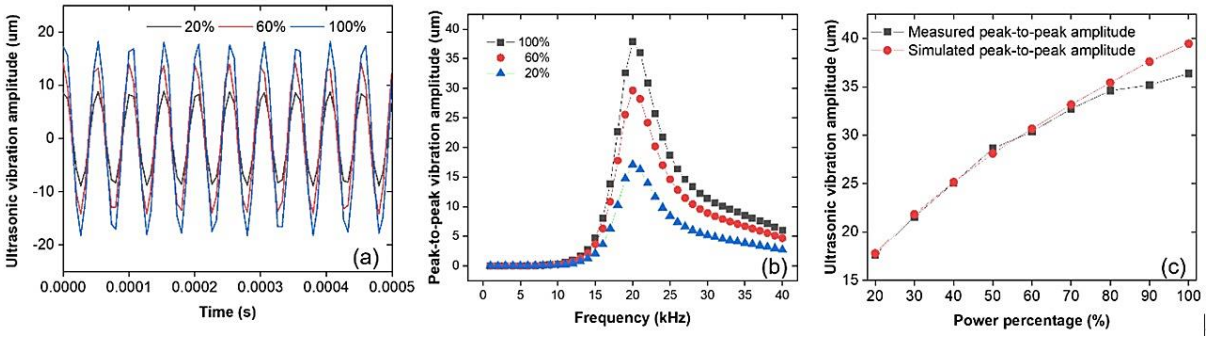

Figure 39. (a) Measured ultrasonic vibration amplitudes at 20%, 60%, 100% power levels; (b) Simulated peak-to-peak vibration amplitude versus the frequency of the electrical alternation; (c) A comparison between simulated and measured peak-to-peak ultrasonic vibration amplitudes at different power levels.

A comparison between simulated and measured peak-to-peak vibration amplitude is presented in Figure 39(c). The simulated vibration amplitudes at different input electrical power levels agree well with measurements in general. The two simulated vibration amplitudes at high electrical power levels (90%, 100%) are slightly greater than the measurements. A possible reason is that the model does not take the upper limit of ultimate strength of the piezoelectric ceramics into consideration. The high input electrical power levels (90%, 100%) might exceed the maximum allowable electrical field to the piezoelectric ceramics, resulting in the fluctuation of amplitude measurements. This difference is also reported in the literature [70].

3.1.3. Results and Discussion

3.1.3.1. Acoustic Intensity Distribution

Figure 40 demonstrates the simulated instantaneous acoustic intensity distribution in a biomass volume. High acoustic intensity (up to 10^6 W/m^2) is found in the close vicinity of the ultrasonic horn. As ultrasound waves travel through biomass, acoustic intensity is attenuated along the propagating direction (z axis), and ultrasound energy is absorbed by the medium and result in heat generation.

Figure 41 describes the acoustic intensity evolution along the z axis at different power levels. It is noted that the z axis is defined as the axis passing through the center of the biomass volume from biomass top surface. Figure 41 shows that a higher power percentage produces a higher acoustic intensity. As the ultrasound wave propagates through the biomass, the acoustic intensity decreases with the distance from the ultrasonic horn due to attenuation.

The volumetric heat generation rate due to absorption can be modeled in the relationship with the acoustic intensity I and absorption α as shown in Equation (41). So, most of the heating occurs in the upper region of biomass volume due to the local high acoustic intensity, and a temperature elevation occurs because of the resultant heat generation.

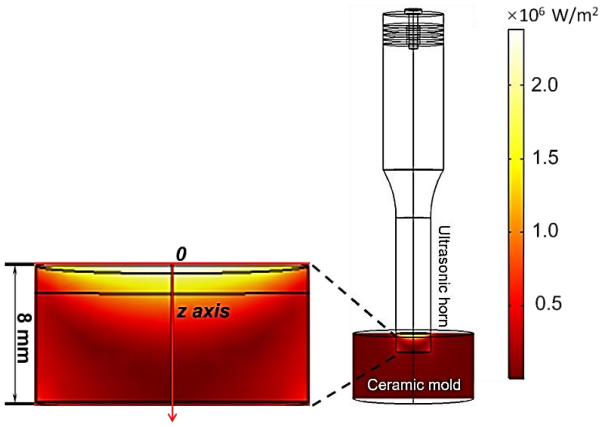

Figure 40. Simulated acoustic intensity distribution in a biomass volume

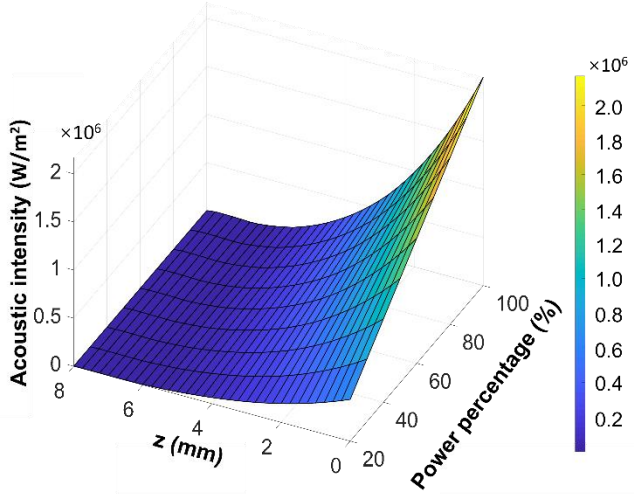

Figure 41. The acoustic intensity along z axis at different input power levels

3.1.3.2. Temperature Distribution

Figure 42 demonstrates the temperature distribution at 15, 30, 45, and 60 second of torrefaction, respectively. It shows that the temperature can reach to as high as 573K (300°C) in the upper region of biomass volume and the temperature on the side boundaries can also reach 380K (107°C) at the end of 60 second. Torrefaction is a mild pyrolysis process, in which biomass is thermally degraded at temperature ranges from 433-573K (160-300°C). At the initial stage (433-453K or 160-180°C), most of the moisture contained in biomass is removed and lignin becomes soft and begins to melt through auto-crosslinking reactions, exhibiting a thermosetting property. When the elevated temperature reaches to 453-573K (180-300°C), the percentage of volatile matters is reduced by decomposing the majority of hemicellulose and some cellulose, it removes the polar hydroxyl and carbonyl groups resulting in the reduction of oxygen-to-carbon (O/C) and hydrogen-to-carbon (H/C) ratios and the increase of fixed carbon content torrefied biomass. These fuel property upgrades make torrefied biomass more compatible with coal for efficient co-combustion.

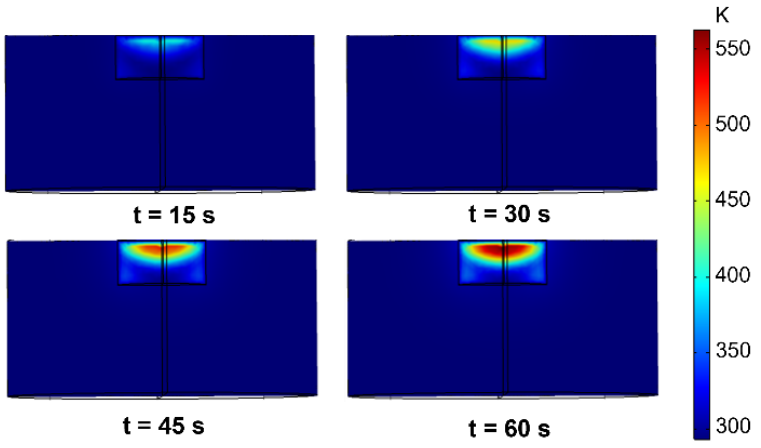

Figure 42. The biomass temperature elevation and spatial distribution at 15s, 30s, 45s, and 60s of ultrasound-assisted torrefaction time (power percentage = 100%)

Figure 43(a) is a depiction of the temperature elevation along z axis with different input electrical powers. It is observed that temperature first rise from top surface (z = 0), then it gets

turn over (z = 1.75 mm) and falls gradually towards the bottom (z = 8 mm). The highest temperature at varying power levels is remained at the same location (z = 1.75 mm). Figure 43(b) shows a representative computation of temperature elevation during 60 s at different locations along z axis. The temperature rapidly increases to 473-573K (200-300°C) in the upper regions of the biomass volume, which is at the needed temperature regimes to realize certain torrefaction severity levels, while it increases gradually on the lower regions, and barely changes at the bottom surface.

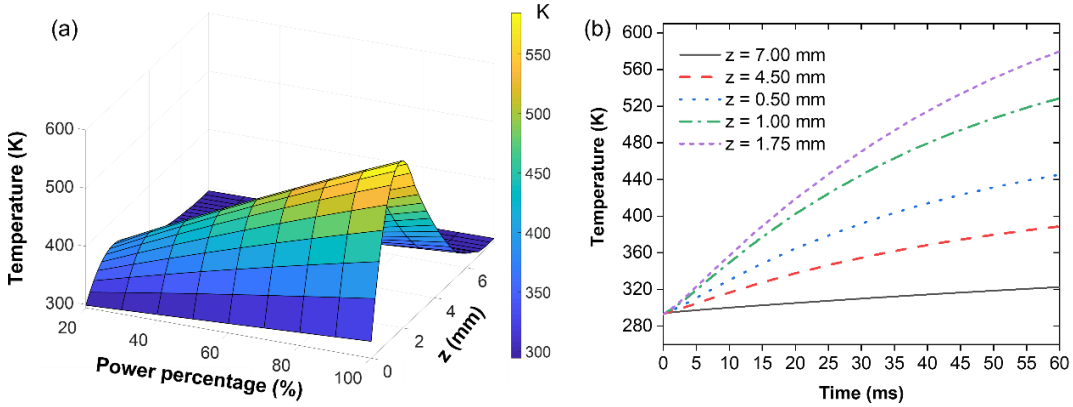

Figure 43. (a) Simulated temperature profiles over time at different locations (power percentage = 100%); (b) The temperature profiles along z axis at different power levels.

Temperature at the pellet center was measured at different ultrasonic power levels by an embedded thermocouple and compared with predicted temperature as shown in Figure 44. The simulated temperature elevation trend is consistent with experimental results, indicating a good prediction accuracy of this model.

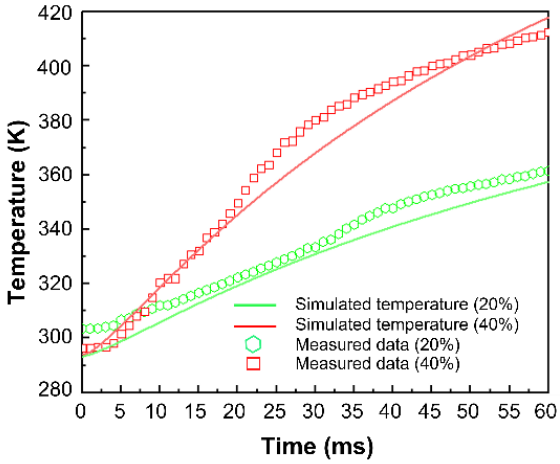

Figure 44. A comparison between the simulated and measured temperature

3.1.4. Conclusion

In this presented work, ultrasound-assisted torrefaction was studied by both theoretical modeling and experimental investigation. A physics-based temperature model was developed to investigate the effects of ultrasonic power and torrefaction duration on temperature elevation in a volume of biomass. The simulation of the ultrasonic horn vibration was first validated to verify that this model can capture the vibration characteristic of the 20 kHz ultrasonic system used in this study. The temperature at the center of the biomass was also measured to validate the model's temperature prediction. Both simulated and experimental results indicate that ultrasonic power has a significant effect on the volumetric heating rate. Generally, simulated temperature grows as ultrasonic power increases. This temperature rise tendency agrees with the experimental results. Both experimental and simulated results suggest that ultrasound-assisted torrefaction can produce torrefied biomass fuel pellet within 60 seconds.

3.2. Biomass Viscoelastic Heating

3.2.1. Model Description

3.2.1.1. The Generalized Maxwell Model

Biomass mainly consists of three polymers: cellulose, hemicellulose, and lignin. These polymers are associated with each other in a hetero-matrix to different degrees; Biomass polymer matrix can be considered a viscoelastic material (Figure 45), which exhibits both viscous and elastic characteristics when undergoing deformation. When ultrasonic vibration is applied together with a perpendicular pelletizing force onto biomass, the biomass is subjected to a high frequency sinusoidal strain and will dissipate energy in the form of heat generation through viscoelastic heating. A viscoelastic heating model was built to predict the temperature distribution inside a biomass pellet. Viscoelastic materials are often modeled as generalized Maxwell solids (Figure 45), a combination of springs and dashpots to present their viscoelastic properties. The generalized Maxwell model is composed of i+1 units in parallel, being i Maxwell units and an isolated spring to warrant solid behavior. A Maxwell unit has a spring and a dashpot connected in series. The spring models the elastic component of the response, while the dashpot represents the viscous component.

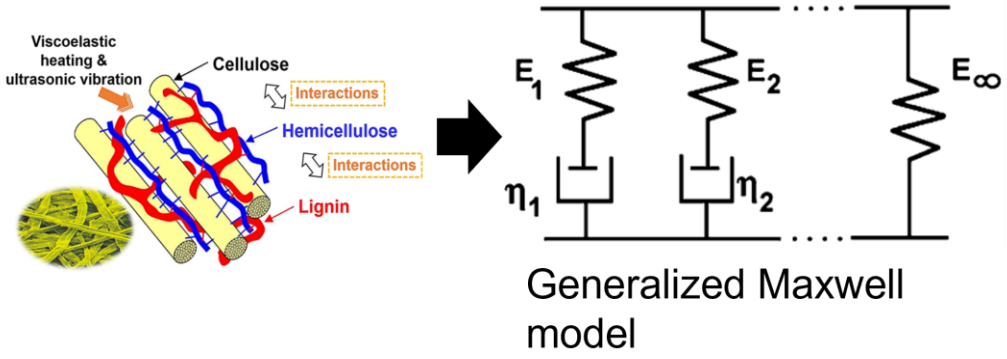

Figure 45. The matrix of three polymers: cellulose, hemicellulose and lignin in biomass

3.2.1.2. Derivation of Volumetric Heat Source

As illustrated in Figure 46, when ultrasonic vibration is applied together with a perpendicular pelletizing force onto biomass, the biomass is subjected to a high-frequency sinusoidal strain and will dissipate energy in the form of heat generation through viscoelastic heating. Biomass polymer matrix can be considered a viscoelastic material and can be modeled as generalized Maxwell model.

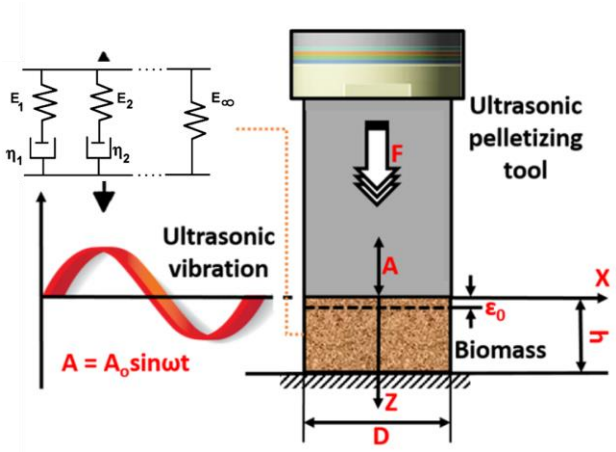

Figure 46. . Illustration of biomass under ultrasonic pelletizing

The basics elements of a Maxwell unit are a spring and a dashpot, as shown in Figure 47 (a) and (b), respectively.

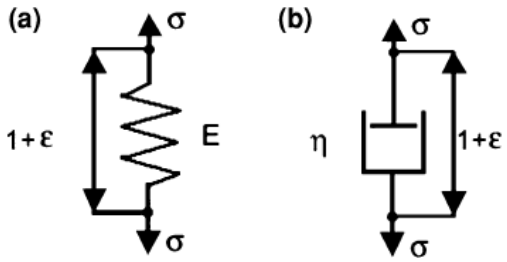

Figure 47. Basic elements of (a) spring and (b) dashpot

An ideal helicoidal spring represents Hooke model (Equation (43)), where *E* is the elasticity modulus:

$$\sigma(t) = E \cdot \varepsilon(t) \tag{43}$$

The dashpot is an ideal viscous element that extends at a rate proportional to the applied stress, where η is the viscosity coefficient.

$$\sigma(t) = \eta \cdot \dot{\varepsilon}(t) \tag{44}$$

A Maxwell unit combines a spring and a dashpot in series, the equations can be written as:

$$\sigma(t) = \sigma_E(t) = \sigma_\eta(t) \tag{45}$$

$$\varepsilon(t) = \varepsilon_E(t) + \varepsilon_\eta(t) \tag{46}$$

The strain is the same for all Maxwell units. And the total stress is the sum of each Maxwell unit. Combining Equation (43) - (46), the differential equation can be determined as:

$$\dot{\varepsilon}(t) = \frac{\dot{\sigma}(t)}{E} + \frac{\sigma(t)}{\eta} \tag{47}$$

In the case of the dynamic response, Equation (47) gives:

$$E(i\omega)\varepsilon_0^* \exp(i\omega t) = \left(i\omega + \frac{1}{\tau}\right)\sigma_0^* \exp(i\omega t),\ \tau = \frac{\eta}{E} \tag{48}$$

$$E^* = \frac{\sigma_0^*}{\varepsilon_0^*} = \frac{E(i\omega\tau)}{1+i\omega\tau} = \frac{E\omega^2\tau^2}{1+\omega^2\tau^2} + i\frac{E\omega\tau}{1+\omega^2\tau^2} \tag{49}$$

The complex modulus E* of Generalized Maxwell model is then:

$$E^* = E'(\omega) + iE''(\omega) = \left[E_\infty + \sum_{r=1}^{n}\left(\frac{E_r\omega^2{\tau_r}^2}{1+\omega^2{\tau_r}^2}\right)\right] + i\left[\sum_{r=1}^{n}\frac{E_r\omega\tau_r}{1+\omega^2\tau_r^2}\right] \tag{50}$$

$$\begin{aligned} E'(\omega) &= E_\infty + \sum_{r=1}^{n}\left(\frac{E_r\omega^2{\tau_r}^2}{1+\omega^2{\tau_r}^2}\right) \\ E''(\omega) &= \sum_{r=1}^{n}\frac{E_r\omega\tau_r}{1+\omega^2\tau_r^2} \end{aligned} \tag{51}$$

E’ is the in-phase or elastic response, proportional to the recoverable or stored energy; E” is the out-of-phase or viscous response, proportional to the irrecoverable or dissipated energy.

If the strain function is written as:

$$\varepsilon = \varepsilon_0 \cos \omega t \tag{52}$$

The stress function as a complex quantity σ∗:

$$\sigma^* = \sigma_0^{'} \cos \omega t + i\sigma_0^{"} \sin \omega t \tag{53}$$

The strain energy per unit volume done:

$$W = f \oint \sigma(t) d\varepsilon(t) \tag{54}$$

Integrating the in-phase and out-of-phase components separately:

$$\begin{aligned} W &= f \oint \sigma(t) d\varepsilon(t) \\ &= f \int_0^{\frac{2\pi}{\omega}} \left(\sigma_0^{'} \cos \omega t\right)\left(-\varepsilon_0 \omega \sin \omega t\right) dt + \int_0^{\frac{2\pi}{\omega}} \left(\sigma_0^{"} \sin \omega t\right)\left(-\varepsilon_0 \omega \sin \omega t\right) dt \\ &= f\left(0 - \pi \sigma_0^{"} \varepsilon_0\right) \end{aligned} \tag{55}$$

The net dissipation, which is the volumetric heat generation rate *Q* can be reformulated as:

$$Q = f \pi \varepsilon_0^2 E^{"} \tag{56}$$

Taking the attenuation of the ultrasonic amplitude into consideration, the ultrasonic vibration amplitude function in the propagation direction z is given by [71-72]:

$$A(z,t) = A_0 e^{-\alpha z} \times \exp\left\{ i\omega\left(t - \frac{z}{c} \right) \right\} \tag{57}$$

Where *A* is the vibration amplitude, *c* is the propagation speed of sound, and *α* is the attenuation factor as shown in followed:

$$\alpha = \frac{\omega \tan \delta}{c} z = \omega z \frac{\omega E^{"}}{E^{'}} \sqrt{\frac{\rho}{E^{'}}} \tag{58}$$

The volumetric heat generation rate is obtained by combining Equations (56)-(58):

$$Q(z) = f\varepsilon_0^2 \exp\left\{\frac{-2E^{''}\omega z}{E^{'}\sqrt{\frac{\rho}{E^{'}}}}\right\} \tag{59}$$

A spatial-temporal temperature distribution inside a biomass pellet can be solved by following the governing differential equation:

$$k_x \frac{\partial^2 T}{\partial x^2} + k_y \frac{\partial^2 T}{\partial y^2} + k_z \frac{\partial^2 T}{\partial z^2} + Q(T, \omega, z) - \rho C(T) \frac{\partial T}{\partial t} = 0 \tag{60}$$

where ρ is biomass density; C(T) is specific heat capacity as a function of temperature; and k_x, k_y, and k_z are heat conductivity in three coordinate directions.

3.2.1.3. Complex Modulus of Biomass Polymer

It is known that viscoelastic heating depends mainly upon material viscoelastic moduli, deformation range, and applied deformation frequency. The viscoelastic properties of different biomass materials, including storage modulus (E'), loss modulus (E"), complex modulus (E*), and loss factor ($tan\delta$), have to be characterized first. This paper used numerical approximation approaches to fit the temperature-dependent and frequency-dependent functions using published DMA data.

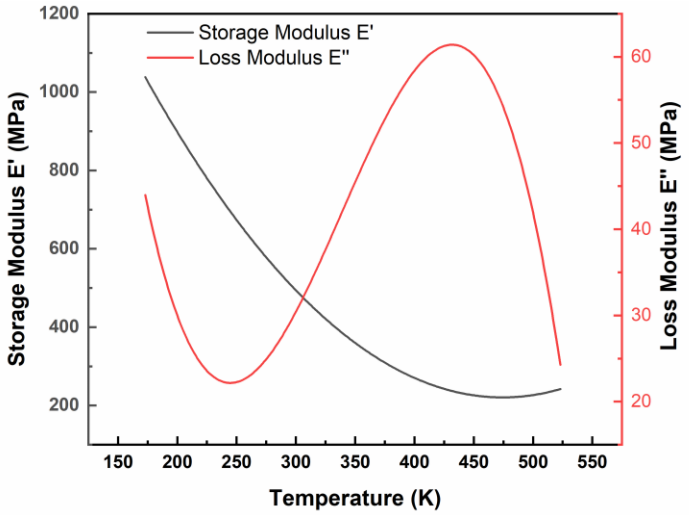

Figure 48. Regression model of wheat straw storage/loss modulus

So far, the viscoelastic heating rate $Q\ (T, \omega, z)$ as a function of temperature, frequency, and location is established. The values of parameters in this model is listed in Table 4.

Table 4. Parameters and values in modelling synchronized ultrasonic torrefaction and pelleting

Parameter	Value
c	340 m/s
ρ	1 kg/m^3
h	6 $W/(m^2K)$
t	60 s
f	10, 15, 20, 25 kHz
ε_0	2.25×10^{-3}, 2.5×10^{-3}, 3.12×10^{-3}, 3.50×10^{-3}

3.2.1.4. Thermal Boundary Conditions

Figure 49 shows a schematic illustration of the mold filled with biomass particles and fully densified. W_2, W_3, and W_4 represent external boundaries; W_1, W_5 and W_6 are internal boundaries.

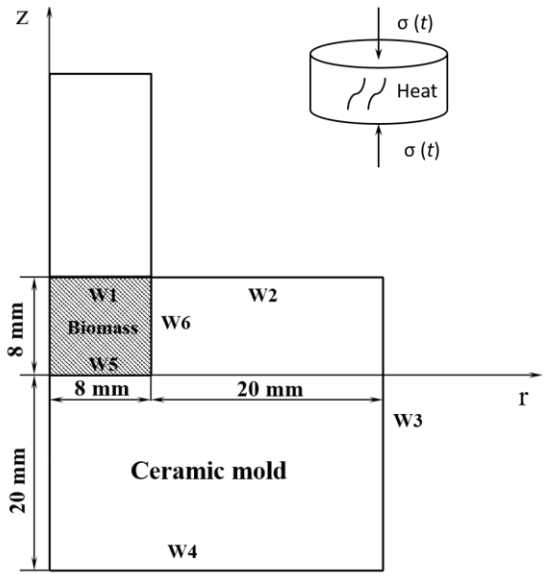

Figure 49. Simplified loading condition of biomass and (b) A schematic illustration of temperature model

The governing differential equations are solved based on the boundary conditions described below:

(1) Initial condition:

$$T_{W7} = T_0 \tag{61}$$

(2) External boundary conditions:

$$-\lambda_2\left(\frac{\partial T_{W2}}{\partial z}\right) = h\left(T_{W2} - T_f\right)\ \left(t \geq 0,\ z = 8{,}8 \leq r < 28\right) \tag{62}$$

$$-\lambda_2\left(\frac{\partial T_{W3}}{\partial r}\right) = h\left(T_{W3} - T_f\right)\ \left(t \geq 0,\ z = 28, -20 \leq r < 8\right) \tag{63}$$

$$-\lambda_2\left(\frac{\partial T_{W4}}{\partial z}\right) = h\left(T_{W4} - T_f\right)\ \left(t \geq 0,\ z = -20, 0 \leq r < 28\right) \tag{64}$$

$$-\lambda_2\left(\frac{\partial T_{W8}}{\partial z}\right) = h\left(T_{W8} - T_f\right)\ \left(t \geq 0,\ z = 8{,}8 \leq r < 28\right) \tag{65}$$

(3) Internal boundary conditions:

$$-\lambda_1\left(\frac{\partial T_1}{\partial z}\right)_{W1} = -\lambda_2\left(\frac{\partial T_2}{\partial z}\right)_{W1} \tag{66}$$

$$-\lambda_1\left(\frac{\partial T_1}{\partial z}\right)_{W5} = -\lambda_2\left(\frac{\partial T_2}{\partial z}\right)_{W5} \tag{67}$$

$$-\lambda_1\left(\frac{\partial T_1}{\partial r}\right)_{W6} = -\lambda_2\left(\frac{\partial T_2}{\partial r}\right)_{W1} \tag{68}$$

3.2.2. Results and Discussion

3.2.2.1. Temperature Distribution

The process of synchronized ultrasonic torrefaction and pelleting is simulated as biomass undergoes a high frequency strain under a constant pelleting pressure. As shown in Figure 50, when the vibration frequency is 20 kHz, ultrasonic amplitude is 25 um (40% ultrasonic power), and pelleting pressure is 20 psi, the simulated temperature at pellet center reaches about 499 K, and the simulated temperature along r direction drops with increasing distance from pellet center. The reason for this relationship is that the heat exchange performance is weakened at pellet center compared to that at the boundary.

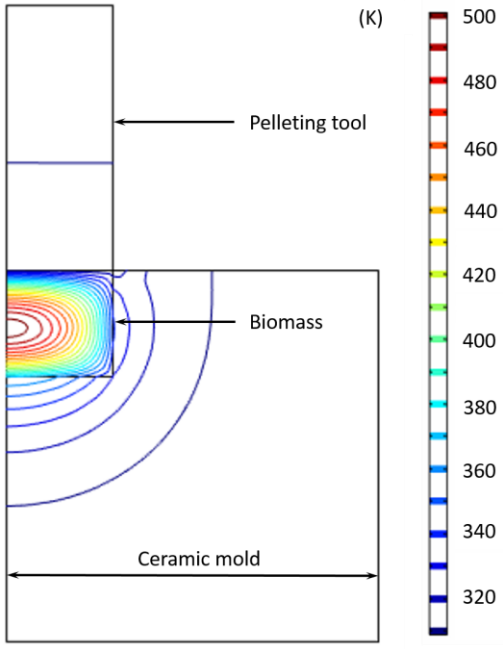

Figure 50. Predicted temperature distribution (ultrasonic amplitude = 25 um, pressure = 20 psi)

Figure 51 demonstrates the 3-dimensional temperature distributions at 15 s, 30 s, 45 s, and 60 s of pelleting time, respectively. It shows that pellet center is most effectively torrefied during the synchronized ultrasonic torrefaction and pelleting process, and the temperature on the pellet boundary can also reaches about 380k at 60 s. Comparing the simulation and experimental

results shown in Figure 52, the predicted temperature (499 K) at pellet center is close to the experimental result (479 K), and the simulated trend of temperature increase rate agrees with that obtained from experiments.

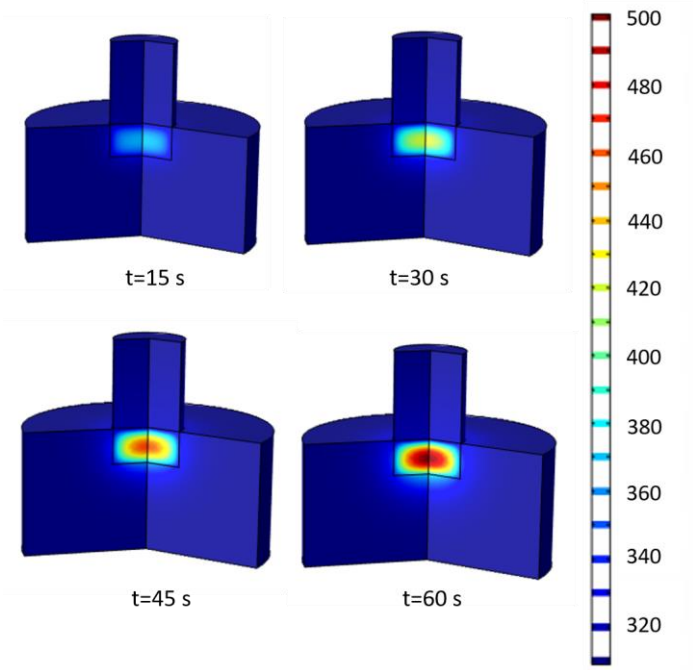

Figure 51. Predicted temperature change over time (ultrasonic amplitude = 25 um, pressure = 20 psi)

Figure 53 shows the simulated temperature profiles at pellet top, center, and bottom surfaces when the vibration frequency is 20 kHz, ultrasonic amplitude is 25 um. It can be observed that temperature increases rapidly at pellet center caused by viscoelastic heating in the biomass, while it increases gradually on pellet top surface due to viscoelastic heating together with heat convection. Besides, temperature barely changes on pellet bottom surface because of the low heat conductivity of the ceramic mold.

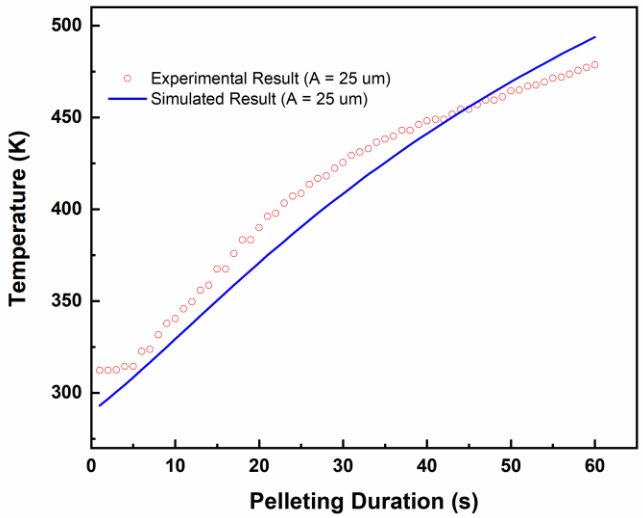

Figure 52. Comparison of experimental and simulated results of the pellet center temperature

The phenomenon mentioned above can be also depicted in Figure 54, which is the temperature profile at the symmetric z axis along the pellet center. It demonstrates that temperature goes up from pellet top surface to pellet center, reaching to the highest temperature, and falls from pellet center to bottom.

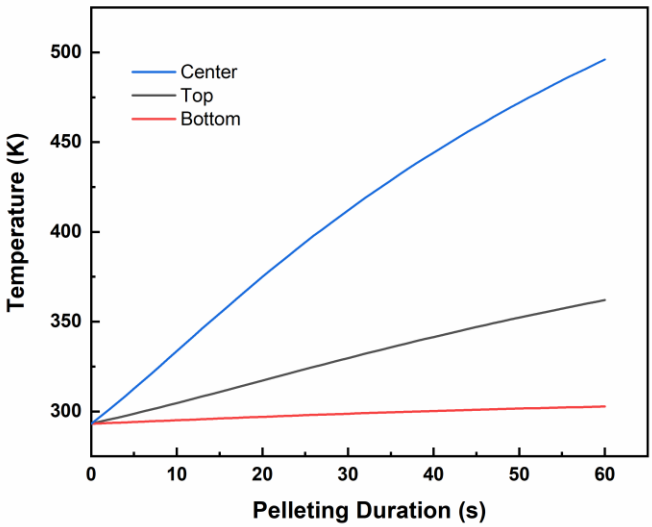

Figure 53. Temperature over time at pellet top, center and bottom surfaces

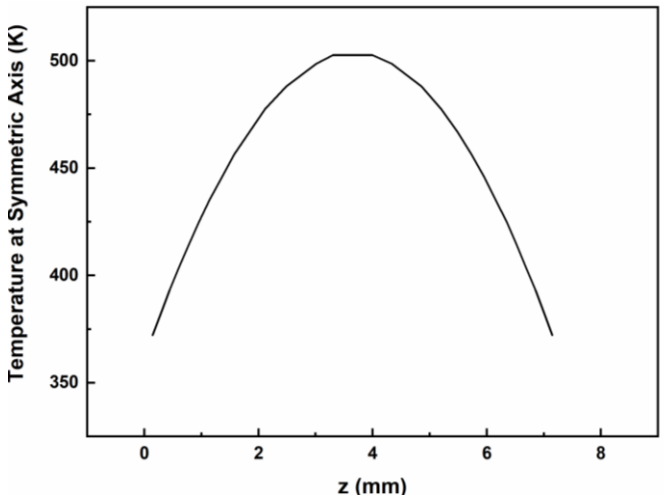

Figure 54. Temperature profile at the symmetric axis

3.2.2.2. Effects of Ultrasonic Amplitude on Temperature

Figure 55 shows the measured and simulated temperature change over time at pellet center under different ultrasonic amplitudes, which are 18 um, 20 um, and 25 um, respectively. It is demonstrated that higher temperature increase rate is achieved when the ultrasonic amplitude is greater.

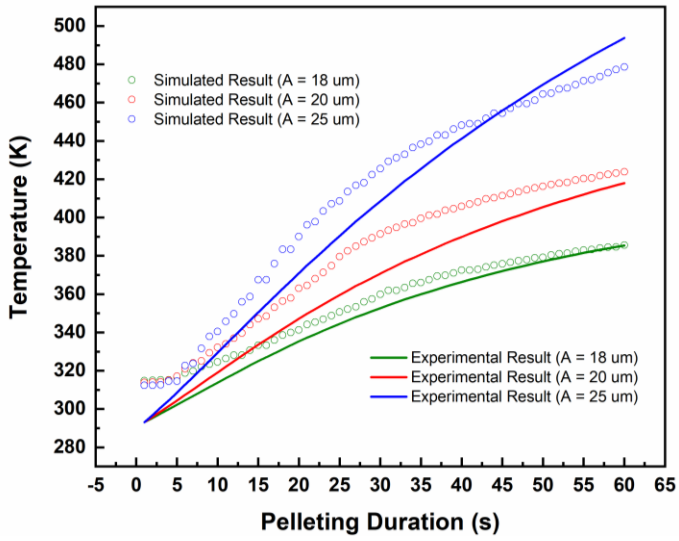

Figure 55. Comparison of experimental and simulated results of the pellet center temperature at different ultrasonic amplitude

Figure 56 demonstrates the simulated temperature at the pellet center at 60 s under different ultrasonic amplitudes. Temperature at pellet center grows as ultrasonic amplitude increases, illustrating that ultrasonic amplitude has a significant influence on volumetric viscoelastic heating rate.

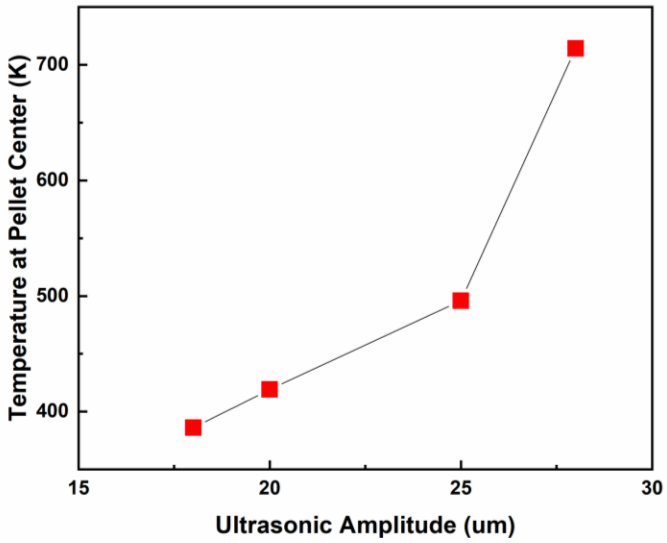

Figure 56. The influence of ultrasonic amplitude on temperature at the pellet center

3.2.2.3. Effects of Ultrasonic Frequency on Temperature

Figure 57 shows the influence of the ultrasonic frequency (10 kHz, 15 kHz, 20 kHz, 25 kHz) on temperature. It can be observed that the ultrasonic frequency is also an important parameter that has a significant influence on viscoelastic heating rate (temperature). Since the adjustment of ultrasonic frequency is not available in our experimental system, the simulated results were not validated by experiments. From Equation (59), it is known that viscoelastic heating rate is linearly proportional to ultrasonic frequency.

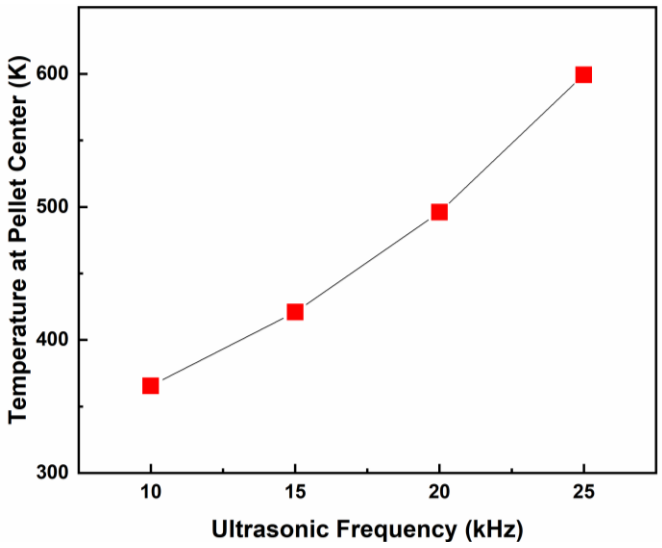

Figure 57. The influence of ultrasonic frequency on temperature at the pellet center

The viscoelastic heating mechanism of biomass during synchronized ultrasonic torrefaction and pelleting was studied by both theoretical modelling and experimental investigation. A physics-based temperature model, with the attenuation of ultrasonic amplitude in biomass taken into consideration, was developed as an expression of ultrasonic frequency, ultrasonic amplitude, biomass storage modulus, and biomass loss modulus for synchronized ultrasonic torrefaction and pelleting. The temperature model was then employed in COMSOL. The effects of process parameters, including ultrasonic amplitude, ultrasonic frequency, pelleting duration, and location were investigated and were validated by experimentally measured temperature data.

Both simulated and experimental results indicate that ultrasonic amplitude has a significant effect on the volumetric viscoelastic heating rate. Generally, simulated pellet center temperature grows as ultrasonic amplitude increases. This temperature rise tendency agrees with the experimental results. The simulated effects of ultrasonic frequency on viscoelastic heating rate indicates that viscoelastic heating rate is linearly proportional to ultrasonic frequency. It is

predicted that the temperature at pellet center can achieve to a range of 365-600 K in less than 60 s when the frequency is in the range of 10 kHz to 25 kHz. This temperature range is sufficient for the occurrence of torrefaction and depolymerization of major biomass compositions.

In conclusion, viscoelastic heating is the predominant heat source in synchronized ultrasonic torrefaction and pelleting of biomass. Moreover, this model can help to understand the fuel upgrading mechanism of synchronized ultrasonic torrefaction and pelleting and to give instructions for process optimization to produce high quality fuel pellets.

3.2.3. Conclusion

The viscoelastic heating mechanism of biomass during synchronized ultrasonic torrefaction and pelleting was studied by both theoretical modelling and experimental investigation. A physics-based temperature model, with the attenuation of ultrasonic amplitude in biomass taken into consideration, was developed as an expression of ultrasonic frequency, ultrasonic amplitude, biomass storage modulus, and biomass loss modulus for synchronized ultrasonic torrefaction and pelleting. The temperature model was then employed in COMSOL. The effects of process parameters, including ultrasonic amplitude, ultrasonic frequency, pelleting duration, and location were investigated and were validated by experimentally measured temperature data.

Both simulated and experimental results indicate that ultrasonic amplitude has a significant effect on the volumetric viscoelastic heating rate. Generally, simulated pellet center temperature grows as ultrasonic amplitude increases. This temperature rise tendency agrees with the experimental results. The simulated effects of ultrasonic frequency on viscoelastic heating rate indicates that viscoelastic heating rate is linearly proportional to ultrasonic frequency. It is predicted that the temperature at pellet center can achieve to a range of 365-600 K in less than 60 s when the frequency is in the range of 10 kHz to 25 kHz. This temperature range is sufficient for the occurrence of torrefaction and depolymerization of major biomass compositions.

In conclusion, viscoelastic heating is the predominant heat source in synchronized ultrasonic torrefaction and pelleting of biomass. Moreover, this model can help to understand the fuel upgrading mechanism of synchronized ultrasonic torrefaction and pelleting and to give instructions for process optimization to produce high quality fuel pellets.

Chapter 4 - Conclusions of Synchronized Ultrasonic Torrefaction and Pelleting

This work presents an integrated solution, synchronized ultrasonic torrefaction and pelleting, to producing torrefied pellets that only requires a single material loading. When ultrasonic vibration is applied together with a perpendicular pelletizing force onto biomass, the biomass is subjected to a high-frequency sinusoidal strain and exhibits viscoelastic properties. It is hypothesized that viscoelastic heating induced by ultrasonic vibration makes synchronized torrefaction and pelletizing happen. A simplified temperature model with predicted temperature distribution plotted in Section 3.1. This model depicts the piezoelectric effect of a transducer, the vibration amplitude at the output end of the ultrasonic horn, and the acoustic intensity and temperature distributions in the biomass medium and assumes that the ultrasonic energy is absorbed by biomass and converted into heat. The simplified model serves as a bottom line to compare with the viscoelastic heating temperature model in Section 3.2.

Results show that the viscoelastic heating model is validated by thermocouple measurements, and the predicted temperatures match the needed temperature regimes to realize certain torrefaction severity levels. It is essential to understand the heating mechanism of synchronized ultrasonic torrefaction and pelleting, which will give guidelines for process optimization to produce high quality fuel pellets and add to the literature of both ultrasonics and biomass pre-processing research disciplines.

This work fills up the knowledge gap when biomass torrefaction and pelletizing take place simultaneously. But very limited knowledge is available about the underlying mechanism by which torrefaction improves the thermal and hygroscopic properties of biomass, this will be the next step toward future study.

Chapter 5 - Future Research

5.1. Understanding Thermal Property Improvements

Pellets produced by synchronized torrefaction and pelletizing showed a much higher heating value (HHV) than that of non-torrefied pellets. The fixed carbon content of torrefied pellets was also found to be over 10% higher compared to non-torrefied pellets. It has been widely reported that biomass energy density strongly depends on its fixed carbon content and biomass energy density increases proportionally with the increase of fixed carbon content as predicted by a number of regression models in the literature. When the temperature elevates during synchronized torrefaction and pelletizing, the percentage of volatile matters in biomass is reduced, which should increase the fixed carbon content in torrefied pellets. This will also increase the fuel ratio (carbon to volatile matter contents) of biomass and decrease the reactivity of torrefied pellets. This effect can lead to a more stable combustion process of torrefied pellets compared to the non-torrefied pellets made from raw biomass. In the same manner, the torrefaction process can reduce the oxygen to carbon (O/C) and hydrogen to carbon (H/C) ratios in biomass and make torrefied pellets more compatible with coal for efficient co-combustion.

Biomass elemental and compositional analyses will be conducted in future studies. Torrefied and non-torrefied pellets of different biomass materials will be produced at different ultrasonic power levels. Heating values of pellets will be measured by a bomb calorimeter; biomass elemental analyses will be performed on a CHNOS analyzer, and biomass compositional analyses will be conducted. Close attention will be paid to the following aspects: (1) the difference in carbon, oxygen, and hydrogen contents between torrefied and non-torrefied pellets; (2) the difference in biomass composition (hemicellulose, lignin, and cellulose) between torrefied and non-torrefied pellets; and (3) the difference in crystalline structure of cellulose and

hemicellulose before and after synchronized torrefaction and pelletizing. Furthermore, thermogravimetric (TG) analysis will be employed to provide a comparison of mass loss at different levels of torrefaction severity. In addition, a mass and energy balance study will be performed to understand how biomass energy density is affected by biomass elemental and compositional changes.

5.2. Understanding Hygroscopic Property Improvements

Experimental results show that torrefied pellets absorbed a substantially lower amount of water compared to that by non-torrefied pellets. It is hypothesized that biomass hygroscopic nature changes to hydrophobic due to the removal of hydroxyl groups during synchronized torrefaction and pelletizing. Driven by this hypothesis, FT-IR spectra of torrefied pellets and raw biomass will be obtained and compared at peaks associated with biomass hygroscopic properties. Close attention will be paid to the hydrophilic O-H bond peak at 3300-3400 cm-1, which is associated with the rupture of hemicellulose and cellulose hydrogen bonds. If biomass produced by synchronized torrefaction and pelletizing shows a less intensive O-H bond peak, it will indicate that free and intermolecular bonded hydroxyl groups in raw biomass are partially removed by torrefaction. The removal of the hydrophilic O-H bond can also be supported if the torrefied biomass has a lower hydrogen content from the elemental analysis.

References

[1] P. Kiefer, V. Hahn, M. Nardi, et al., “Sensitive photoresists for rapid multiphoton 3D laser micro- and nanoprinting,” Adv. Opt. Mater., vol. 2000895, pp. 1–14, 2020.

[2] Chen, Yong, and Anne Pepin. "Nanofabrication: Conventional and nonconventional methods." Electrophoresis 22, no. 2 (2001): 187-207.

[3] M. Göppert-Mayer, “Über Elementarakte mit zwei Quantensprüngen,” Ann. Phys., vol. 401, no. 3, pp. 273–294, 1931.

[4] M. Farsari, G. Filippidis, and C. Fotakis, “Fabrication of threedimensional structures by three-photon polymerization,” Opt. Lett., vol. 30, no. 23, pp. 3180–3182, 2005.

[5] Geng, Qiang, Dien Wang, Pengfei Chen, and Shih-Chi Chen. "Ultrafast multi-focus 3-D nano-fabrication based on two-photon polymerization. "Nature communications 10, no. 1 (2019): 1-7.

[6] Uppal, Nitin, and Panos S. Shiakolas. "Modeling of temperature-dependent diffusion and polymerization kinetics and their effects on two-photon polymerization dynamics." Journal of Micro/Nanolithography, MEMS, and MOEMS 7, no. 4 (2008): 043002.

[7] Uppal, Nitin. "A mathematical model development and sensitivity analysis of two photon polymerization for 3D micro/nano fabrication." (2008).

[8] Sun, Hong-Bo, and Satoshi Kawata. "Two-photon photopolymerization and 3D lithographic microfabrication." In NMR• 3D Analysis• Photopolymerization, pp. 169-273. Springer, Berlin, Heidelberg, 2004.

[9] Stampfl, Jürgen, Robert Liska, and Aleksandr Ovsianikov. Multiphoton lithography: Techniques, materials, and applications. John Wiley & Sons, 2016.

[10] Malinauskas, Mangirdas, Maria Farsari, Algis Piskarskas, and Saulius Juodkazis. "Ultrafast laser nanostructuring of photopolymers: A decade of advances." Physics Reports 533, no. 1 (2013): 1-31.

[11] Zhou, Xiaoqin, Yihong Hou, and Jieqiong Lin. "A review on the processing accuracy of twophoton polymerization." AIP Advances 5, no. 3 (2015): 030701.

[12] Lee, Kwang-Sup, Dong-Yol Yang, Sang Hu Park, and Ran Hee Kim. "Recent developments in the use of two-photon polymerization in precise 2D and 3D microfabrications." Polymers for advanced technologies 17, no. 2 (2006): 72-82

[13] Juodkazis, Saulius, Vygantas Mizeikis, and Hiroaki Misawa. "Three-dimensional microfabrication of materials by femtosecond lasers for photonics applications." Journal of Applied Physics 106, no. 5 (2009): 8.

[14] Yang, Liang, Dongdong Qian, Chen Xin, Zhijiang Hu, Shengyun Ji, Dong Wu, Yanlei Hu, Jiawen Li, Wenhao Huang, and Jiaru Chu. "Two-photon polymerization of microstructures by a non-diffraction multifoci pattern generated from a superposed Bessel beam." Optics letters 42, no. 4 (2017): 743-746.

[15] Kawata, Satoshi, Hong-Bo Sun, Tomokazu Tanaka, and Kenji Takada. "Finer features for functional microdevices." Nature 412, no. 6848 (2001): 697-698.

[16] Kohler, Manfred, Jorg Ohngemach, Gregor Wehner, and Jurgen Gehlhaus. "Photoinitiators for photopolymerization of unsaturated systems." U.S. Patent 4,861,916, issued August 29, 1989.

[17] Andey, Ramji. "Photopolymers in 3D printing applications." (2014).

[18] Chen, Mao, Mingjiang Zhong, and Jeremiah A. Johnson. "Light-controlled radical polymerization: Mechanisms, methods, and applications." Chemical reviews 116, no. 17 (2016): 10167-10211.

[19] Gauvin, Robert, Ying-Chieh Chen, Jin Woo Lee, Pranav Soman, Pinar Zorlutuna, Jason W. Nichol, Hojae Bae, Shaochen Chen, and Ali Khademhosseini. "Microfabrication of complex porous tissue engineering scaffolds using 3D projection stereolithography." Biomaterials 33, no. 15 (2012): 3824-3834.

[20] Mann, Brenda K., Andrea S. Gobin, Annabel T. Tsai, Rachael H. Schmedlen, and Jennifer L. West. "Smooth muscle cell growth in photopolymerized hydrogels with cell adhesive and proteolytically degradable domains: synthetic ECM analogs for tissue engineering." Biomaterials 22, no. 22 (2001): 3045-3051.

[21] Oakdale, James S., Raymond F. Smith, Jean-Baptiste Forien, William L. Smith, Suzanne J. Ali, Leonardus B. Bayu Aji, Trevor M. Willey et al. "Direct laser writing of low-density interdigitated foams for plasma drive shaping." Advanced Functional Materials 27, no. 43 (2017): 1702425.

[22] Farsari, Maria, and Boris N. Chichkov. "Two-photon fabrication." Nature photonics 3, no. 8 (2009): 450-452.

[23] Bauer, Jens, Almut Schroer, Ruth Schwaiger, and Oliver Kraft. "Approaching theoretical strength in glassy carbon nanolattices." Nature materials 15, no. 4 (2016): 438-443.

[24] Gissibl, Timo, Simon Thiele, Alois Herkommer, and Harald Giessen. "Two-photon direct laser writing of ultracompact multi-lens objectives." Nature photonics 10, no. 8 (2016): 554-560.

[25] Turner, Mark D., Matthias Saba, Qiming Zhang, Benjamin P. Cumming, Gerd E. Schröder-Turk, and Min Gu. "Miniature chiral beamsplitter based on gyroid photonic crystals." Nature Photonics 7, no. 10 (2013): 801-805.

[26] Vizsnyiczai, Gaszton, Lóránd Kelemen, and Pál Ormos. "Holographic multi-focus 3D two-photon polymerization with real-time calculated holograms." Optics express 22, no. 20 (2014): 24217-24223.

[27] Saha, Sourabh K., Dien Wang, Vu H. Nguyen, Yina Chang, James S. Oakdale, and Shih-Chi Chen. "Scalable submicrometer additive manufacturing." Science 366, no. 6461 (2019): 105-109.

[28] Cheng, He, Chun Xia, Meng Zhang, Stephen M. Kuebler, and Xiaoming Yu. "Fabrication of high-aspect-ratio structures using Bessel-beam-activated photopolymerization." Applied optics 58, no. 13 (2019): D91-D97.

[29] Yu, Xiaoming, Meng Zhang, and Shuting Lei. "Multiphoton polymerization using femtosecond Bessel beam for layerless three-dimensional printing." Journal of Micro and Nano-Manufacturing 6, no. 1 (2018).

[30] Alda, Javier. "Laser and Gaussian beam propagation and transformation." Encyclopedia of optical engineering 999 (2003).

[31] Cheng, He, Chun Xia, Stephen M. Kuebler, and Xiaoming Yu. "Aberration correction for SLM-generated Bessel beams propagating through tilted interfaces." Optics Communications 475 (2020): 126213.

[32] Cheng, He, Chun Xia, Meng Zhang, Stephen M. Kuebler, and Xiaoming Yu. "Fabrication of high-aspect-ratio structures using Bessel-beam-activated photopolymerization." Applied optics 58, no. 13 (2019): D91-D97.

[33] J. B. Mueller, J. Fischer, Y. J. Mange, T. Nann, and M. Wegener, “Insitu local temperature measurement during three-dimensional direct laser writing,” Appl. Phys. Lett., vol. 103, p. 123107, 2013.

[34] Schafer, K.J., et al., Two-photon absorption cross-sections of common photoinitiators. Journal of Photochemistry and Photobiology A: Chemistry, 2004. **162**(2-3): p. 497-502.

[35] Marien, Y.W., et al., Estimating the photodissociation quantum yield from PLP-SEC peak heights. Polymer Chemistry, 2017. **8**(20): p. 3124-3128.

[36] Yang, L., et al., On the Schwarzschild Effect in 3D Two-Photon Laser Lithography. Advanced Optical Materials, 2019. **7**(22): p. 1901040.

[37] Anseth, K.S., C.M. Wang, and C.N. Bowman, Reaction behaviour and kinetic constants for photopolymerizations of multi (meth) acrylate monomers. Polymer, 1994. **35**(15): p. 3243-3250.

[38] Matheson, M.S., et al., Rate Constants in Free Radical Polymerizations. IV. Methyl Acrylate1. Journal of the American Chemical Society, 1951.**73**(11): p. 5395-5400.

[39] Mueller JB, Fischer J, Mange YJ, Nann T, Wegener M. In-situ local temperature measurement during three-dimensional direct laser writing. Applied Physics Letters. 2013 Sep 16;103(12):123107. https://doi.org/10.1063/1.4821556.

[40] Bauer, Jens, Anna Guell Izard, Yunfei Zhang, Tommaso Baldacchini, and Lorenzo Valdevit. "Programmable mechanical properties of two-photon polymerized materials: from nanowires to bulk." Advanced Materials Technologies 4, no. 9 (2019): 1900146.

[41] International Energy Agency (IEA). World Energy Outlook. 2011.

[42] Rahman, Saidur, Abdelaziz, E.A., Demirbas, Ayhan H., Hossain, Monowar S. and Mekhilef, Saad. “A Review on Biomass as A Fuel for Boiler.” Renewable Sustainable Energy Reviews Vol. 15 No. 5 (2011): pp. 2262-2289. DOI: doi.org/10.1016/j.rser.2011.02.015.

[43] Özbay, Nurgul, Pütün, Ayse E., Uzun, Basak B. and Pütün, Ersan. “Biocrude from Biomass: Pyrolysis of Cottonseed Cake.” Renewable Energy Vol. 24 No. 3-4 (2001): pp. 615-625. DOI: doi.org/10.1016/S0960-1481(01)00048-9.

[44] Kambo, Harpreet S. and Dutta, Animesh. “Strength, Storage, and Combustion Characteristics of Densified Lignocellulosic Biomass Produced via Torrefaction and Hydrothermal Carbonization.” Applied Energy Vol. 135 (2014): pp. 182-191. DOI: doi.org/10.1016/j.apenergy.2014.08.094.

[45] Vanderstelt, M.J.C., Gerhauser, H., Kiel, Jacob H.A. and Ptasinski, Krzysztof J. “Biomass Upgrading by Torrefaction for The Production of Biofuels: A Review.” Biomass and Bioenergy Vol. 35 No. 9 (2011): pp. 3748-6372. DOI: doi.org/10.1016/j.biombioe.2011.06.023.

[46] Chew, Jiuan J. and Doshi, Veena A. “Recent Advances in Biomass Pretreatment-Torrefaction Fundamentals and Technology.” Renewable and Sustainable Energy Reviews Vol. 15 No. 8 (2011): pp. 4212-4222. DOI: doi.org/10.1016/j.rser.2011.09.017.

[47] Tran, Khanh Q., Luo, Xun, Seisenbaeva, Gulaim, Jirjis, Raida. “Stump Torrefaction for Bioenergy Application.” Applied Energy Vol. 112 (2013): pp. 539-546. DOI: doi.org/10.1016/j.apenergy.2012.12.053.

[48] Bergman, P.C.A. “Combined Torrefaction and Pelletisation.” The TOP process (2005). URL: https://www.ecn.nl/docs/library/report/2005/c05073.pdf.

[49] Mani, S., Tabil, L. and Sokhansanj, S. “Compaction of Biomass Grinds - An Overview of Compaction of Biomass Grinds.” Powder Handling and Processing Vol. 15 (2003): pp. 160-168.

[50] Theerarattananoon, Karnnalin, Xu, Feng, Wilson, Jonathan, Ballard, R., Mckinney, Leland and Staggenborg, Scott. “Physical Properties of Pellets Made from Sorghum Stalk, Corn Stover, Wheat Straw, and Big Bluestem.” Industrial Crops and Produts Vol. 33 No. 2 (2011): pp. 325-332. DOI: doi.org/10.1016/j.indcrop.2010.11.014.

[51] Reza, Toufiq, Uddin Helal, Lynam Joan and Coronella, Charles. “Engineered Pellets from Dry Torrefied and HTC Biochar Blends.” Biomass and Bioenergy Vol. 63 (2014): pp. 229-38. DOI: doi.org/10.1016/j.biombioe.2014.01.038.

[52] Mani, Sudhagar, Tabil, Lope and Sokhansanj, Shahab. “An Overview of Compaction of Biomass Grinds.” Powder Handling and Processing Vol. 15 No. 3 (2003): pp. 160-168.

[53] Sun, Mingman, Yang, Yang and Zhang, Meng. “A Temperature Model for Synchronized Ultrasonic Torrefaction and Pelleting of Biomass for Bioenergy Production.” International Manufacturing Science and Engineering Conference. MSEC2018-6600: pp. V004T03A042. College Station, TX. 2018. DOI: 10.1115/MSEC2018-6600.

[54] Faborode, Michael. “Analysis of Extrusion Compaction of Fibrous Agricultural Residues for Fuel Applications.” Biomass Vol. 21 No. 2 (1990): pp. 115-128. DOI: doi.org/10.1016/0144-4565(90)90053-M.

[55] Reece, Floyd. “Temperature, Pressure, and Time Relationships in Forming Dense Hay Wafers.” Transactions of the ASAE Vol. 9 No. 6 (1966): PP. 749-0751. DOI: 10.13031/2013.40086.

[56] Rubin, Edward. “Genomics of cellulosic biofuels.” Nature Vol. 454 No. 7206 (2008): pp. 841.

[57] Mosier, Nathan, Charles Wyman, Bruce Dale, Richard Elander, Y. Y. Lee, Mark Holtzapple, and Michael Ladisch. "Features of promising technologies for pretreatment of lignocellulosic biomass."Bioresource technology 96, no. 6 (2005): 673-686.

[59] Shankar Tumuluru, Jaya, Shahab Sokhansanj, J. Richard Hess, Christopher T. Wright, and Richard D. Boardman. "A review on biomass torrefaction process and product properties for energy applications." Industrial Biotechnology 7, no. 5 (2011): 384-401.

[60] Chen, Wei-Hsin, Bo-Jhih Lin, Yu-Ying Lin, Yen-Shih Chu, Aristotle T. Ubando, Pau Loke Show, Hwai Chyuan Ong et al. "Progress in biomass torrefaction: Principles, applications and challenges."Progress in Energy and Combustion Science 82 (2021): 100887.

[61] Stelte, Wolfgang, Anand R. Sanadi, Lei Shang, Jens K. Holm, Jesper Ahrenfeldt, and Ulrik B. Henriksen. "Recent developments in biomass pelletization–A review." BioResources 7, no. 3 (2012): 4451-4490.

[62] Banks, Harvey Thomas, Shuhua Hu, and Zackary R. Kenz. "A brief review of elasticity and viscoelasticity for solids." Advances in Applied Mathematics and Mechanics 3, no. 1 (2011): 1-51.

[63] Marques, Severino PC, and Guillermo J. Creus. Computational viscoelasticity. Springer Science & Business Media, 2012.

[64] Lapasin, Romano, and Sabrina Pricl. "Rheology." In Rheology of industrial polysaccharides: Theory and applications, pp. 162-249. Springer, Boston, MA, 1995.

[65] Macosko Christopher. Rheology: Principles, Measurements, and Applications. Wiley (1994).

[66] Ferry John. Viscoelastic Properties of Polymers. John Wiley & Sons (1980).

[67] Clarke, R.L. and Ter Haar, G.R. (1997). Temperature rise recorded during lesion formation by high-intensity focused ultrasound. Ultrasound in medicine & biology 23(2), 299-306.

[68] Sun, M., Yang, Y. and Zhang, M. (2019). A temperature model for synchronized ultrasonic torrefaction and pelleting of biomass for bioenergy production. Journal of Energy Resources Technology 141(10).

[69] Song, X., Yu, X., Zhang, M., Pei, Z., and Wang, D. (2014). A physics-based temperature model for ultrasonic vibration-assisted pelleting of cellulosic biomass. Ultrasonics 54, 7 (2014): 2042-2049.

[70] Yao, Y. and Liu, S. (2014). Ultrasonic technology for desiccant regeneration. Shanghai, Shanghai Jiao Tong University Press.

[71] Jiang B, Peng H, Wu W, Jia Y, Zhang Y. Numerical simulation and experimental investigation of the viscoelastic heating mechanism in ultrasonic plasticizing of amorphous polymers for micro injection molding. Polymers. 2016;8(5):199-211.

[72] Zhang Z, Wang X, Luo Y. Study on heating process of ultrasonic welding for thermoplastics. Journal of Thermoplastic Composite Materials. 2010;23(5):647-64.